PAPER • OPEN ACCESS

A model for analytical calculations of synthetic neutron energy spectra from beam-target reactions

To cite this article: A. Valentini *et al* 2025 *Nucl. Fusion* **65** 026001

OPEN ACCESS
IOP Publishing | International Atomic Energy Agency
Nuclear Fusion
Nucl. Fusion **65** (2025) 026001 (16pp)
https://doi.org/10.1088/1741-4326/ad9bc8

A model for analytical calculations of synthetic neutron energy spectra from beam-target reactions

A. Valentini[1,2,*], B.C.G. Reman[1,3], M. Nocente[2], J. Eriksson[5], H. Järleblad[4], D. Moseev[6], M. Rud[1], B.S. Schmidt[7], A. Snicker[8] and M. Salewski[1]

[1] Department of Physics, Technical University of Denmark, 2800 Kgs Lyngby, Denmark
[2] Department of Physics, University of Milano-Bicocca, 20126 Milan, Italy
[3] Laboratory for Plasma Physics, LPP-ERM/KMS, Brussels B-1000, Belgium
[4] Department of Appl. Math. & Computer Science, Technical University of Denmark, 2800 Kgs Lyngby, Denmark
[5] Department of Physics and Astronomy, Uppsala University, 75120 Uppsala, Sweden
[6] Max-Planck-Institut fur Plasmaphysik, Wendelsteinstr. 1, Greifswald 17491, Germany
[7] Department of Physics and Astronomy, University of California, Irvine, CA 92697, United States of America
[8] VTT, Technical Research Centre of Finland, Espoo, Finland

E-mail: anvalen@dtu.dk

Received 8 May 2024, revised 19 October 2024
Accepted for publication 9 December 2024
Published 18 December 2024

Abstract

We present a fully analytical model for calculating energy spectra of neutrons generated by fusion reactions involving a fast ion, or beam, and a stationary ion, or target, in magnetic fusion plasmas. For neutrons moving along the line-of-sight of a detector, the neutron spectrum is given by an analytical expression and the usual differential cross section. This makes the model several orders of magnitude faster than ordinary Monte Carlo simulations and free of any related statistical noise. Additionally, the analytical description of the reaction physics provides much more insight into the formation of the spectrum. An example of this is the bias of beam-target spectra towards high-energy neutron counts, which corresponds to forward-emission events. On the other hand, the fast-ion uniform gyro-angle distribution has an opposite effect, but is ultimately weaker than the preferential forward emission of neutrons. The model is validated against numerical calculations from the forward model code GENESIS to verify its validity and it is furthermore derived from a probabilistic viewpoint, adding further insight.

Keywords: fast ions, nuclear reactions, neutron emission spectroscopy

(Some figures may appear in colour only in the online journal)

* Author to whom any correspondence should be addressed.

1. Introduction

On the road to achieving self-sustaining fusion plasmas, the role of so-called 'fast ions'—generated by external heating or fusion reactions directly—is pivotal. In velocity space, these non-thermal populations lie in the tail of the energy distribution, with energies up to the MeV range. In addition to providing heat to the bulk plasma through the slowing-down process [1, 2], they can interact with magnetohydrodynamic instabilities by driving or suppressing them [3, 4]. Much work has been and still is being done on detecting, simulating and analysing these fast populations. Detection techniques are particularly relevant to have a measurement of the distribution function [5–7]. Knowing the physics of neutron emission, one can formulate a forward model, or synthetic diagnostic, and compare computed and measured spectra. Given several simultaneous measurements, tomographic inversion of the measurements using the forward model is also possible [8–11].

In the prospect of reactor-scale experiments, an important diagnostic for fusion plasmas is neutron emission spectroscopy (NES), which relies on the detection and spectral resolution of fusion neutrons. These detection systems are passive and detect neutrons along the line-of-sight, and they are characterized by a signal-to-noise ratio that scales well with the size of the fusion plasma. Several different types of spectrometers exist that measure various quantities that are related to the neutron energy. Two examples are the time-of-flight neutron spectrometers [12] and diamond detectors [7, 13] that measure the energy deposited by a neutron in a diamond crystal. In this work, we illustrate a novel method to calculate neutron spectra due to one-step fusion reactions of a fast ion and a second reactant at rest, sometimes referred to as beam-target reactions. We focus on the deuterium-tritium reaction, but the same formalism can treat any one-step beam-target reaction. We will show that our formalism agrees with Monte Carlo simulations for beam-target reactions where the target reactant is at rest. Since our method does not require Monte Carlo sampling [14, 15], it is considerably faster and leads to noise-free signals. Monte Carlo methods are preferable whenever the motion of both the reactants needs to be accounted for, where a finite temperature of the target distribution generally leads to a broadening of the spectral shape. Our analytical framework can be directly applied to NES measurements of any kind (e.g. time-of-flight, diamond, liquid scintillator) [16], to one-step gamma-ray spectra [17], as well as proton energy spectra [18], and could be extended to work for two-step gamma-ray spectra [19], too.

The work is organized as follows: in section 2, we study the kinematics of the reaction and the emission mechanisms, in the case of a beam-target reaction. In section 3 the expression for the spectrum due to a cold ring distribution [20] is derived from the total neutron rate. Additionally, we discuss the finite resolution of experimental diagnostics and the change of rest frame needed for evaluating the angular probability of the emission. In section 4, a comparison of our calculated spectra with spectra from the Monte Carlo code GENESIS [21, 22] is shown, along with a parametric study on the spectral shape, including the effect of finite temperature of the target particles. Finally, in section 5, we present a complementary derivation from a probabilistic viewpoint, providing further insight. In section 6, we discuss possible applications of the model. Section 7 presents our conclusions.

2. Kinematics of the DT reaction with tritium at rest

Neutrons in the MeV range can be generated via fusion reactions. In magnetic plasma confinement fusion research the two most common reactions are the neutronic branch of the DD fusion reaction, i.e. $\mathfrak{D} + \mathrm{D} \rightarrow {}^3\mathrm{He} + \mathrm{n}$, and the DT fusion reaction

$$\mathfrak{D} + \mathrm{T} \longrightarrow \alpha + \mathrm{n}\,. \tag{1}$$

The calligraphic font in equation (1) indicates the fast species in the beam-target reaction, i.e. the deuterium is fast and the tritium is stationary. We choose to focus on fast deuterium colliding with tritium at rest since this reaction is the dominant contribution to the fusion energy yield obtained during the DTE2 campaign [23] at the Joint European Torus (JET).

To understand the spectrum formation in NES measurements, we start with the kinematics of one-step fusion reactions [5, 17, 24]. We focus on classical calculations here as it provides the most clear and tractable model and refer to [25] for the more accurate relativistic extension of this model. In the beam-target case, the discrepancy observed is a rigid shift of the neutron energy that depends on the Q-value of the reaction ($\sim$20 keV for DT neutrons). For reactants with Maxwellian distributions, the relativistic corrections are thoroughly studied in [26–28] instead.

In the case of second reactant at rest, the neutron energy E_n along a selected direction depends only on the velocity of the fast reactant. This dependence is implied by the conservation of energy and momentum, which in the laboratory frame are—for a fast deuterium reacting with a stationary tritium (with $\boldsymbol{v}_\mathrm{T} = \boldsymbol{0}$)—

$$m_\mathfrak{D}\boldsymbol{v}_\mathfrak{D} = m_\alpha \boldsymbol{v}_\alpha + m_\mathrm{n}\boldsymbol{v}_\mathrm{n}\,, \tag{2}$$

$$\frac{1}{2}m_\mathfrak{D}v_\mathfrak{D}^2 + Q = \frac{1}{2}m_\alpha v_\alpha^2 + \frac{1}{2}m_\mathrm{n}v_\mathrm{n}^2\,. \tag{3}$$

Since we seek to calculate synthetic neutron energy spectra, given a velocity distribution function of the fast deuterium $f_\mathfrak{D}$, we take the deuterium velocity $\boldsymbol{v}_\mathfrak{D}$ as known. Equations (2) and (3) then constitute a set of 4 equations for 6 unknowns. If we further impose that the neutron must move along the line-of-sight of a given neutron emission spectrometer, the motion of the neutron is described fully by its speed, such that we only have 4 unknowns. To obtain an equation for the neutron speed, we isolate v_α in equation (2) and substitute it into equation (3), which gives

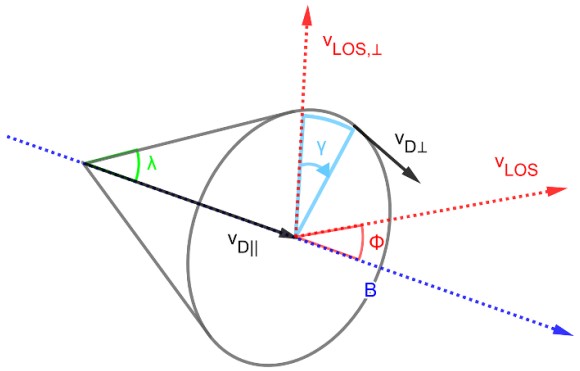

Figure 1. Schematic drawing of gyro-motion in terms of ion velocities, with respect to the local magnetic field line and to the LOS, in 3D. Unit vectors are shown as dotted lines.

$$E_{\mathfrak{D}} + Q = \frac{1}{2m_\alpha}\left(m_{\mathfrak{D}}\boldsymbol{v}_{\mathfrak{D}} - m_{\mathrm{n}}\boldsymbol{v}_{\mathrm{n}}\right)^2 + \frac{m_{\mathrm{n}}}{2}v_{\mathrm{n}}^2 = \frac{1}{2m_\alpha}\left(m_{\mathfrak{D}}^2 v_{\mathfrak{D}}^2 + m_n^2 v_{\mathrm{n}}^2 - 2m_{\mathfrak{D}}m_{\mathrm{n}}\boldsymbol{v}_{\mathfrak{D}}\cdot\boldsymbol{v}_{\mathrm{n}}\right) + \frac{m_{\mathrm{n}}}{2}v_{\mathrm{n}}^2 \,. \tag{4}$$

In this step, the projection of the fast ion velocity $\boldsymbol{v}_{\mathfrak{D}}$ onto the neutron emission direction $\hat{\boldsymbol{v}}_n$ appears, given that

$$\boldsymbol{v}_{\mathfrak{D}}\cdot\boldsymbol{v}_{\mathrm{n}} = v_{\mathrm{n}}\boldsymbol{v}_{\mathfrak{D}}\cdot\hat{\boldsymbol{v}}_{\mathrm{n}} \equiv v_{\mathrm{n}}u_{\mathfrak{D}} \,, \tag{5}$$

where we define $u_{\mathfrak{D}}$ as the fast ion projected velocity. This quantity is key to understand the formation of energy spectra in NES [5], as it governs the up- or down-shift of the energy of the detected product, and similarly for other spectroscopic fast-ion diagnostics. This concept applies broadly in the field of fast ion spectroscopy independently on the measurement principle. In a magnetized plasma, we can describe the deuterium velocity by its speed $v_{\mathfrak{D}}$, the pitch angle $\lambda_{\mathfrak{D}}$ and the gyro-angle $\gamma_{\mathfrak{D}}$. The projected velocity along a line-of-sight with observation angle ϕ to the local magnetic field $\boldsymbol{B}$ is then given by [29]

$$u_{\mathfrak{D}} = v_{\mathfrak{D}\parallel}\cos\phi - v_{\mathfrak{D}\perp}\sin\phi\sin\gamma_{\mathfrak{D}} = v_{\mathfrak{D}}\left(\cos\lambda_{\mathfrak{D}}\cos\phi - \sin\lambda_{\mathfrak{D}}\sin\phi\sin\gamma_{\mathfrak{D}}\right) \,, \tag{6}$$

where $v_{\mathfrak{D}\parallel}$ is the fast ion velocity component parallel to $\boldsymbol{B}$, and $v_{\mathfrak{D}\perp}$ is the component perpendicular to $\boldsymbol{B}$. Figure 1 illustrates the fast ion gyration and neutron emission for generic values of $\lambda_{\mathfrak{D}}$ and ϕ.

Combining equations (4)–(6) yields a relation between the gyro-angle $\gamma_{\mathfrak{D}}$ and neutron energy $E_{\mathrm{n}} = m_{\mathrm{n}}v_{\mathrm{n}}^2/2$ for given energy $E_{\mathfrak{D}}$ and pitch $\cos\lambda_{\mathfrak{D}}$ of the fast deuterium and observation angle ϕ [24]:

$$\sin\gamma_{\mathfrak{D}} = \frac{-\left(m_\alpha + m_{\mathrm{n}}\right)E_{\mathrm{n}} + \left(m_\alpha - m_{\mathfrak{D}}\right)E_{\mathfrak{D}} + m_\alpha Q}{2\sqrt{m_{\mathfrak{D}}E_{\mathfrak{D}}m_{\mathrm{n}}E_{\mathrm{n}}}\sin\lambda_{\mathfrak{D}}\sin\phi} + \frac{\cos\lambda_{\mathfrak{D}}\cos\phi}{\sin\lambda_{\mathfrak{D}}\sin\phi} \,. \tag{7}$$

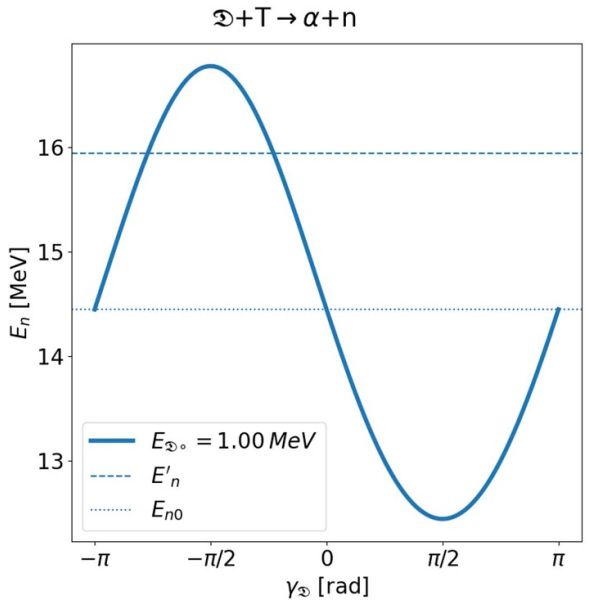

Figure 2. Detected neutron energy as a function of the fast ion gyro-angle on an entire gyro-orbit. The horizontal dashed line indicates an arbitrary value of the neutron energy, while the horizontal dotted line indicates the nominal energy.

Since $\sin\gamma_{\mathfrak{D}} \in [-1,1]$, equation (7) gives the possible range of neutron energies. Additionally, we notice that the same neutron energy value E_{n}' is swept twice by the gyro-angle coordinate $\gamma_{\mathfrak{D}}$ if we consider a full fast ion gyro-orbit. This can also be shown by solving equation (7) for $E_{\mathrm{n}}(\gamma_{\mathfrak{D}})$, which is plotted in figure 2. In the following, we restrict the gyro-angle domain to $\gamma_{\mathfrak{D}} \in [-\pi/2, \pi/2]$ (see figure 3) and refer to equation (7) as a one-to-one mapping between $\gamma_{\mathfrak{D}}$ and E_{n}.

In the next section, we introduce cold ring distributions to evaluate the 'building block' of any neutron energy spectrum [30].

3. Neutron energy spectrum from a fast deuterium cold ring

3.1. Derivation from total neutron rate

In order to evaluate a neutron energy spectrum, we first consider the total neutron rate produced by two reactant populations described by the distribution functions $f_{\mathfrak{D}}$ and f_{T}. We evaluate this quantity from a position $\boldsymbol{r}$ in the plasma as [31]

$$\left(\frac{\mathrm{d}n}{\mathrm{d}t}\right)_{\mathrm{tot}} = \int \sigma_{\mathrm{lab}}\left(v_{\mathrm{rel}}\right)v_{\mathrm{rel}}f_{\mathfrak{D}}\left(\boldsymbol{v}_{\mathfrak{D}},\boldsymbol{r}\right)f_{\mathrm{T}}\left(\boldsymbol{v}_{\mathrm{T}},\boldsymbol{r}\right)\mathrm{d}\boldsymbol{v}_{\mathfrak{D}}\mathrm{d}\boldsymbol{v}_{\mathrm{T}} \,, \tag{8}$$

where σ_{lab} is the reaction cross section evaluated in the laboratory (lab) frame and $v_{\mathrm{rel}} \equiv |\boldsymbol{v}_{\mathfrak{D}} - \boldsymbol{v}_T|$ is the relative velocity between the fast deuterium $\mathfrak{D}$ and the slow tritium T. Equation (8) determines the rate of neutrons born at any energy E_{n} and emitted in any direction. If we choose the relative velocity $\boldsymbol{v}_{\mathrm{rel}}$ as a reference to define the neutron emission in the

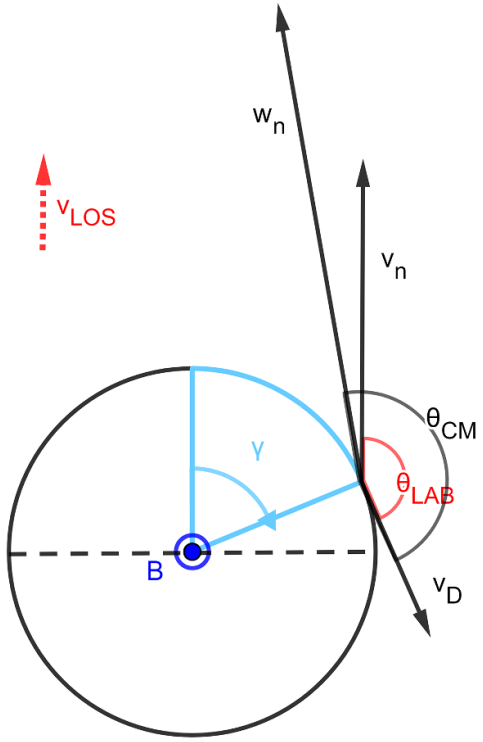

Figure 3. Gyration of a fast ion and neutron emission for the case of co-planar gyration and neutron emission ($\lambda = \pi/2$, $\phi = \pi/2$). The unit vector along the line-of-sight (dotted vector arrow) is parallel to the neutron velocity.

laboratory frame, then this may be defined by a polar angle $\theta_{\rm lab}$ (see figure 3) and an azimuthal angle ψ. Given a detector with a finite physical aperture towards the plasma, the solid angle of the observation cone in spherical coordinates is calculated as [32]

$$\mathrm{d}\Omega_{\rm lab} = \sin\theta_{\rm lab}\mathrm{d}\theta_{\rm lab}\mathrm{d}\psi = -\mathrm{d}\cos\theta_{\rm lab}\mathrm{d}\psi \ . \tag{9}$$

The azimuthal coordinate ψ, when evaluating the emission probability in a cone with solid angle $\mathrm{d}\Omega_{\rm lab}$, is an ignorable coordinate since at relatively low energy ranges (keVs) the scattering is dominated by s-wave processes [33]. Therefore, the differential cross section we need to evaluate the amount of neutrons emitted within a solid angle $\mathrm{d}\Omega_{\rm lab}$ is

$$\begin{aligned}\mathrm{d}\sigma_{\rm lab}\left(\boldsymbol{v}_{\rm rel}\right) &= \frac{\mathrm{d}\sigma\left(\boldsymbol{v}_{\rm rel}\right)}{\mathrm{d}\Omega_{\rm lab}}\mathrm{d}\Omega_{\rm lab} \\ &= \frac{1}{2\pi}\frac{\mathrm{d}\sigma\left(\boldsymbol{v}_{\rm rel}\right)}{\mathrm{d}\cos\theta_{\rm lab}}\mathrm{d}\Omega_{\rm lab} \ ,\end{aligned} \tag{10}$$

such that the total cross section is 2π times the integral of the differential cross section $\mathrm{d}\sigma/\mathrm{d}\cos\theta_{\rm lab}$ over the full interval $\cos\theta_{\rm lab} \in [-1, 1]$. Note that now the cross section depends on the relative velocity vector $\boldsymbol{v}_{\rm rel}$ since the angular distribution of emission is parameterized by $\cos\theta_{\rm lab}$ which is defined with respect to $\hat{\boldsymbol{v}}_{\rm rel}$.

The differential form for the nuclear reaction cross section allows us to evaluate the number of neutrons emitted towards the detector per unit time and unit volume (i.e. the volumetric rate) by accounting for the different reaction probabilities at different directions of emission:

$$\begin{aligned}\frac{\mathrm{d}n}{\mathrm{d}t} = \frac{1}{2\pi}\int \frac{\mathrm{d}\sigma\left(\boldsymbol{v}_{\rm rel}\right)}{\mathrm{d}\cos\theta_{\rm lab}}\mathrm{d}\Omega_{\rm lab}v_{\rm rel}f_{\mathfrak{D}}\left(\boldsymbol{v}_{\mathfrak{D}},\boldsymbol{r}\right) \\ \times f_{\rm T}\left(\boldsymbol{v}_{\rm T},\boldsymbol{r}\right)\mathrm{d}\boldsymbol{v}_{\mathfrak{D}}\mathrm{d}\boldsymbol{v}_{\rm T} \ .\end{aligned} \tag{11}$$

The neutron energy spectrum is then typically derived by integrating over the neutron energy $E_{\rm n}$ and selecting a specific neutron energy $E'_{\rm n}$ at which to evaluate the spectral density of neutrons by means of a Dirac delta function $\delta(E_{\rm n} - E'_{\rm n})$ [31]. This reflects how Monte Carlo simulations calculate energy spectra, as we describe in appendix. For beam-target reactions with stationary target, however, simplifications arise due to the specific distribution functions of the reactants and, in practice, the integral reduces to a function evaluation. If the complete spectrum is predominantly generated by beam-target reactions, one can describe it a as a linear combination of many elementary spectra due to a single 'unit' of fast ions. In velocity space, this unit is referred to as a 'cold ring' distribution [20] and is of the form

$$f_{\mathfrak{D}}\left(v_{\mathfrak{D}},\lambda_{\mathfrak{D}}\right) = \frac{n_{\mathfrak{D}}}{2\pi v_{\mathfrak{D}}^2}\delta\left(v_{\mathfrak{D}} - v_{\mathfrak{D}\circ}\right)\delta\left(\cos\lambda_{\mathfrak{D}} - \cos\lambda_{\mathfrak{D}\circ}\right) \ , \tag{12}$$

where the factor 2π reflects that the gyro-angle $\gamma_{\mathfrak{D}}$ is uniformly distributed, and $n_{\mathfrak{D}} = n_{\mathfrak{D}}(\boldsymbol{r})$ is the local fast-ion density in m^{-3}. The 'ring' subscript for $v_{\mathfrak{D}\circ}$ and $\cos\lambda_{\mathfrak{D}\circ}$ indicates that a velocity (or energy) and a pitch value are selected for that specific cold ring. These distribution functions take their name after the shape they trace in the 3D velocity space $\{v_{\mathfrak{D}\parallel}, v_{\mathfrak{D}\perp 1}, v_{\mathfrak{D}\perp 2}\}$, where $v_{\mathfrak{D}\perp 1}$ and $v_{\mathfrak{D}\perp 2}$ are such that $v_{\mathfrak{D}\perp 1}^2 + v_{\mathfrak{D}\perp 2}^2 = v_{\mathfrak{D}\perp}^2$.

In fact, any fast ion distribution function with uniform gyro-angles can be described in terms of a sum of cold rings and, in the case of beam-target dominated signal, the resulting spectrum can similarly be decomposed into signals originating from cold rings. This idea applies to 2D velocity-space calculations, as well as to 3D synthetic signals in a phase-space of choice—whether it is the 'orbit-space' [34, 35] or the 'constants-of-motion' phase-space [36]—by spatially integrating the generated signal along the diagnostic line-of-sight in the plasma volume.

The stationary tritium T has a velocity $\boldsymbol{v}_{\rm T} = \boldsymbol{0}$ and the corresponding distribution reduces to a point distribution described by

$$f_{\rm T}\left(\boldsymbol{v}_{\rm T}\right) = n_{\rm T}\delta\left(\boldsymbol{v}_{\rm T}\right) \ , \tag{13}$$

where, as in equation (12), the density is local $n_{\rm T} = n_{\rm T}(\boldsymbol{r})$, while the velocity delta function fixes the velocity vector $\boldsymbol{v}_{\rm T}$ to zero $\boldsymbol{0}$. We plug equations (12) and (13) into the integral equation (11) and obtain, after integrating over the velocity of the stationary reactant $\boldsymbol{v}_{\rm T}$

$$\begin{aligned}\frac{\mathrm{d}n}{\mathrm{d}t} = \frac{n_{\mathfrak{D}}n_{\rm T}}{4\pi^2}\int \frac{\mathrm{d}\sigma\left(\boldsymbol{v}_{\mathfrak{D}}\right)}{\mathrm{d}\cos\theta_{\rm lab}}\mathrm{d}\Omega_{\rm lab}v_{\mathfrak{D}}\frac{1}{v_{\mathfrak{D}}^2} \\ \times \delta\left(v_{\mathfrak{D}} - v_{\mathfrak{D}\circ}\right)\delta\left(\cos\lambda_{\mathfrak{D}} - \cos\lambda_{\mathfrak{D}\circ}\right) \\ \times v_{\mathfrak{D}}^2\mathrm{d}v_{\mathfrak{D}}\mathrm{d}\cos\lambda_{\mathfrak{D}}\mathrm{d}\gamma_{\mathfrak{D}} \ ,\end{aligned} \tag{14}$$

where we note that the relative velocity is now given by the velocity of the fast ion $\boldsymbol{v}_\mathfrak{D}$ since $\boldsymbol{v}_\mathrm{T} \approx 0$. Before evaluating the integrals over the deuterium velocity and pitch, we first discuss the differential cross section term. For $v_\mathfrak{D}$, we know that the cross section for a two-body reaction [37] with reduced mass $\mu = (m_\mathfrak{D} m_\mathrm{T})/(m_\mathfrak{D} + m_\mathrm{T})$ and relative kinetic energy $K = \mu v_\mathrm{rel}^2/2 \approx \mu v_\mathfrak{D}^2/2$ is calculated as

$$\sigma\left(v_\mathfrak{D}\right) = \frac{S(K(v_\mathfrak{D}))}{K(v_\mathfrak{D})} \exp\left(-\frac{\beta_\mathrm{G}}{K(v_\mathfrak{D})}\right) , \tag{15}$$

where β_G is the Gamow factor [38] and $S(K(v_\mathfrak{D}))$ is the astrophysical factor, expressed as a ratio of Padé polynomials [37]. For $\lambda_\mathfrak{D}$, $\gamma_\mathfrak{D}$ and ϕ, instead, we need to calculate the cosine of the emission angle $\cos\theta_\mathrm{lab}$ (figure 3) to estimate the angular probability of emitting along a certain direction. This quantity is defined as

$$\cos\theta_\mathrm{lab} = \hat{\boldsymbol{v}}_\mathrm{rel} \cdot \hat{\boldsymbol{v}}_\mathrm{n} \equiv \hat{\boldsymbol{v}}_\mathrm{rel} \cdot \hat{\boldsymbol{v}}_\mathrm{LOS} , \tag{16}$$

where the neutron emission direction coincides with the direction specified by the line-of-sight since the neutron is detected. If we plug in the definition of relative velocity of the reactants and consider the approximation of tritium at rest, we obtain

$$\cos\theta_\mathrm{lab} := \frac{\boldsymbol{v}_\mathfrak{D} - \boldsymbol{v}_T}{|\boldsymbol{v}_\mathfrak{D} - \boldsymbol{v}_T|} \cdot \hat{\boldsymbol{v}}_\mathrm{n} \approx \frac{\boldsymbol{v}_\mathfrak{D}}{|\boldsymbol{v}_\mathfrak{D}|} \cdot \hat{\boldsymbol{v}}_\mathrm{n} = \frac{u_\mathfrak{D}}{v_\mathfrak{D}} , \tag{17}$$

where, in the last step, we make use of the definition of fast ion projected velocity $u_\mathfrak{D}$ from equation (5). Eliminating the projected velocity $u_\mathfrak{D}$ according to equation (6) gives

$$\cos\theta_\mathrm{lab} = \frac{u_\mathfrak{D}}{v_\mathfrak{D}} = \cos\lambda_\mathfrak{D}\cos\phi - \sin\lambda_\mathfrak{D}\sin\phi\sin\gamma_\mathfrak{D} . \tag{18}$$

Since $\lambda_\mathfrak{D}$ and ϕ are fixed, equation (18) shows that $\cos\theta_\mathrm{lab}$ only depends on the gyro-angle $\gamma_\mathfrak{D}$ and can hence also be related to the neutron energy E_n according to equation (7). We note that equation (18) implies that $\cos\theta_\mathrm{lab}$ only covers the entire interval $[-1, 1]$ if $\sin\lambda_\mathfrak{D} = 1$ and $\sin\phi = 1$. If $\sin\lambda_\mathfrak{D} = 0$ or $\sin\phi = 0$, the interval in $\cos\theta_\mathrm{lab}$ reduces to a point. This means that the contribution to the whole spectrum may differ significantly from a certain region of the phase-space to others, depending on the specific differential cross section and the local values of pitch angle and observation angle. From equation (18), the boundary values are obtained by setting $\sin\gamma_\mathfrak{D}$ to ± 1:

$$C_\mathrm{lab}^\pm = \cos\lambda_\mathfrak{D}\cos\phi \mp \sin\lambda_\mathfrak{D}\sin\phi . \tag{19}$$

We can now express the differential cross section by highlighting the parameters that govern the calculation of the emission angle, namely

$$\frac{\mathrm{d}\sigma\left(\boldsymbol{v}_\mathfrak{D}\right)}{\mathrm{d}\cos\theta_\mathrm{lab}} = \frac{\mathrm{d}\sigma\left(v_\mathfrak{D}, \lambda_\mathfrak{D}, \gamma_\mathfrak{D}, \phi\right)}{\mathrm{d}\cos\theta_\mathrm{lab}} , \tag{20}$$

Plugging equation (20) in the integral equation (14), and integrating over $\mathrm{d}v_\mathfrak{D}$ and $\mathrm{d}\cos\lambda_\mathfrak{D}$ gives

$$\frac{\mathrm{d}n}{\mathrm{d}t} = \frac{n_\mathfrak{D} n_\mathrm{T}}{4\pi^2} v_{\mathfrak{D}\circ} \int_{-\pi}^{\pi} \frac{\mathrm{d}\sigma\left(v_{\mathfrak{D}\circ}, \lambda_{\mathfrak{D}\circ}, \gamma_\mathfrak{D}, \phi\right)}{\mathrm{d}\cos\theta_\mathrm{lab}} \mathrm{d}\Omega_\mathrm{lab} \mathrm{d}\gamma_\mathfrak{D} , \tag{21}$$

where the delta functions have now picked out the velocity $v_{\mathfrak{D}\circ}$ and pitch angle $\lambda_{\mathfrak{D}\circ}$ of the cold ring distribution. The remaining degree of freedom is the gyro-angle $\gamma_\mathfrak{D}$, which varies in the interval $[-\pi, \pi]$ (figure 3). We assume the fraction of solid angle to be constant during the gyro-motion at a point $\boldsymbol{r}$ observed from a long distance L away from the plasma [39], i.e.

$$\frac{\mathrm{d}n}{\mathrm{d}t} \approx \frac{\Delta\Omega_\mathrm{lab}}{4\pi^2} n_\mathfrak{D} n_\mathrm{T} v_{\mathfrak{D}\circ} \int_{-\pi}^{\pi} \frac{\mathrm{d}\sigma\left(v_{\mathfrak{D}\circ}, \lambda_{\mathfrak{D}\circ}, \gamma_\mathfrak{D}, \phi\right)}{\mathrm{d}\cos\theta_\mathrm{lab}} \mathrm{d}\gamma_\mathfrak{D} . \tag{22}$$

This approximation is accurate since, in standard magnetic fusion experiments, the gyro-radius is much smaller than the distance to the detector, $r_L \ll L$, such that the solid angle is very small and varies slowly with $\gamma_\mathfrak{D}$. As a result, we will write '=' instead of '≈' sign from here on, for simplicity.

If we consider equation (7) for half a gyro-orbit, i.e. $\gamma_\mathfrak{D} \in [-\pi/2, \pi/2]$, then the detected neutron rate equation (22) can be written as twice the integral over half the gyro-orbit

$$\frac{\mathrm{d}n}{\mathrm{d}t} = \frac{\Delta\Omega_\mathrm{lab}}{2\pi^2} n_\mathfrak{D} n_\mathrm{T} v_{\mathfrak{D}\circ} \int_{-\pi/2}^{\pi/2} \frac{\mathrm{d}\sigma\left(v_{\mathfrak{D}\circ}, \lambda_{\mathfrak{D}\circ}, \gamma_\mathfrak{D}, \phi\right)}{\mathrm{d}\cos\theta_\mathrm{lab}} \mathrm{d}\gamma_\mathfrak{D} , \tag{23}$$

and we can change the integration variable to the neutron energy E_n:

$$\begin{aligned} \frac{\mathrm{d}n}{\mathrm{d}t} = {} & \frac{\Delta\Omega_\mathrm{lab}}{2\pi^2} n_\mathfrak{D} n_\mathrm{T} v_{\mathfrak{D}\circ} \\ & \times \int_{E_\mathrm{n}(\gamma_\mathfrak{D}=-\pi/2)}^{E_\mathrm{n}(\gamma_\mathfrak{D}=\pi/2)} \frac{\mathrm{d}\sigma\left(v_{\mathfrak{D}\circ}, \lambda_{\mathfrak{D}\circ}, \gamma_\mathfrak{D}\left(E_\mathrm{n}\right), \phi\right)}{\mathrm{d}\cos\theta_\mathrm{lab}} \\ & \times \left|\frac{\mathrm{d}\gamma_\mathfrak{D}}{\mathrm{d}E_\mathrm{n}}\right|_{v_{\mathfrak{D}\circ}, \lambda_{\mathfrak{D}\circ}, \phi} \mathrm{d}E_\mathrm{n} . \end{aligned} \tag{24}$$

The Jacobian in equation (24) depends on the variables fixed previously by the Dirac delta functions, and so we indicate it with the same notation as for the cross section. The Jacobian can be conveniently calculated from equation (7) by applying the chain rule

$$\begin{aligned} \left|\frac{\mathrm{d}\gamma_\mathfrak{D}}{\mathrm{d}E_\mathrm{n}}\right| = {} & \left|\frac{\mathrm{d}\gamma_\mathfrak{D}}{\mathrm{d}\sin\gamma_\mathfrak{D}} \frac{\mathrm{d}\sin\gamma_\mathfrak{D}}{\mathrm{d}E_\mathrm{n}}\right| = \frac{1}{\cos\gamma_\mathfrak{D}} \\ & \times \left|\frac{\left(m_\alpha + m_\mathrm{n}\right) E_\mathrm{n} + \left(m_\alpha - m_\mathfrak{D}\right) E_\mathfrak{D} + m_\alpha Q}{4\sqrt{m_\mathfrak{D} E_\mathfrak{D} m_\mathrm{n} E_\mathrm{n}^3} \sin\lambda_\mathfrak{D} \sin\phi}\right| , \end{aligned} \tag{25}$$

where the cosine of the gyro-angle is moved out of the absolute value operator since it is always positive in $[-\pi/2, \pi/2]$. The value of $\cos\gamma_\mathfrak{D}$ is determined by equation (7) using

$$\cos\gamma_\mathfrak{D}\left(E_\mathrm{n}, v_\mathfrak{D}, \lambda_\mathfrak{D}, \phi\right) = \sqrt{1 - \sin^2\gamma_\mathfrak{D}\left(E_\mathrm{n}, v_\mathfrak{D}, \lambda_\mathfrak{D}, \phi\right)} . \tag{26}$$

We can take the derivative of equation (24) with respect to E_n and obtain the volumetric neutron rate per unit energy in the

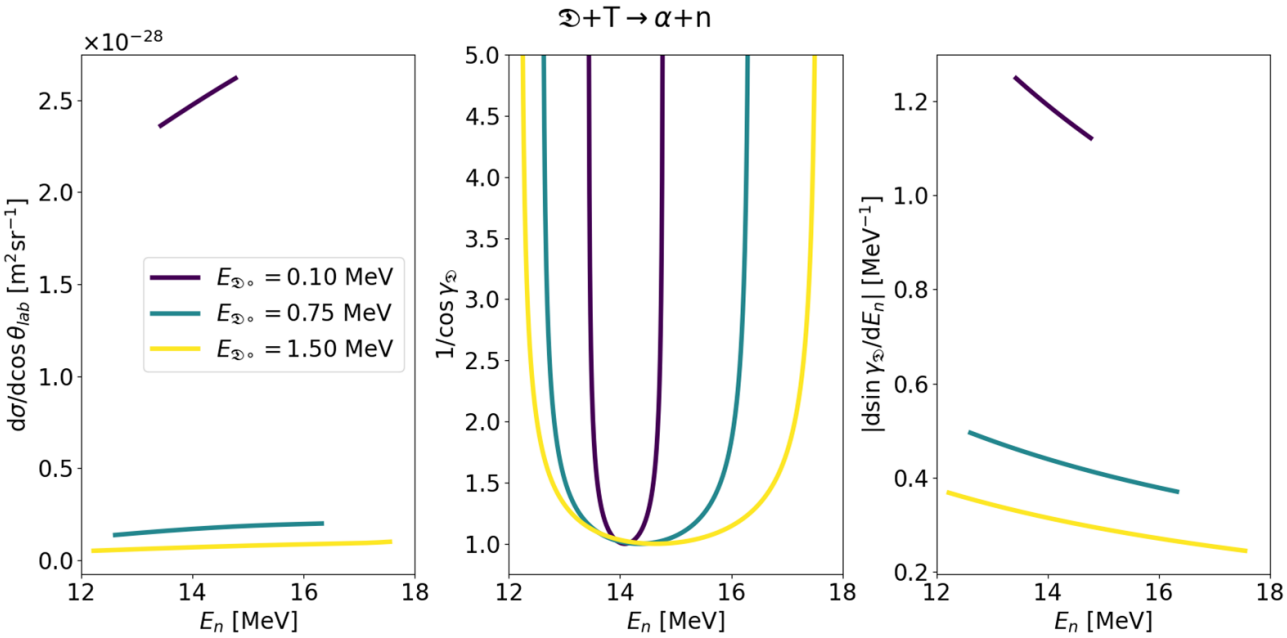

Figure 4. All quantities are expressed in terms of neutron energies $E_{\mathrm{n}\circ}$ and shown for 3 different laboratory frame fast deuterium energies $E_{\mathfrak{D}}$. The cold ring has pitch angle $\lambda_{\mathfrak{D}\circ} = \pi/2$ and is observed with viewing angle $\phi = \pi/2$. From left to right, we can see the laboratory frame differential cross section, the Jacobian term $\mathrm{d}\gamma_{\mathfrak{D}}/\mathrm{d}\sin\gamma_{\mathfrak{D}}$ and the Jacobian term $|\mathrm{d}\sin\gamma_{\mathfrak{D}}/\mathrm{d}E_{\mathrm{n}}|$.

case of a fast deuterium with energy $E_{\mathfrak{D}\circ} = \frac{1}{2} m_{\mathfrak{D}} v_{\mathfrak{D}\circ}^2$ and pitch angle $\lambda_{\mathfrak{D}\circ}$ observed with an angle ϕ:

$$\begin{aligned}\frac{\mathrm{d}^2 n}{\mathrm{d}E_{\mathrm{n}}\mathrm{d}t} &= \frac{\Delta\Omega_{\mathrm{lab}}}{2\pi^2} n_{\mathfrak{D}} n_{\mathrm{T}} v_{\mathfrak{D}\circ} \\ &\quad\times \frac{\mathrm{d}\sigma\left(v_{\mathfrak{D}\circ}, \lambda_{\mathfrak{D}\circ}, \gamma_{\mathfrak{D}}\left(E_{\mathrm{n}}\right), \phi\right)}{\mathrm{d}\cos\theta_{\mathrm{lab}}} \left|\frac{\mathrm{d}\gamma_{\mathfrak{D}}}{\mathrm{d}E_{\mathrm{n}}}\right|_{v_{\mathfrak{D}\circ}, \lambda_{\mathfrak{D}\circ}, \phi} \\ &= \frac{\Delta\Omega_{\mathrm{lab}}}{2\pi^2} n_{\mathfrak{D}} n_{\mathrm{T}} v_{\mathfrak{D}\circ} \frac{\mathrm{d}\sigma\left(v_{\mathfrak{D}\circ}, \lambda_{\mathfrak{D}\circ}, \gamma_{\mathfrak{D}}\left(E_{\mathrm{n}}\right), \phi\right)}{\mathrm{d}\cos\theta_{\mathrm{lab}}} \\ &\quad\times \frac{1}{\cos\gamma_{\mathfrak{D}}\left(E_{\mathrm{n}}, v_{\mathfrak{D}\circ}, \lambda_{\mathfrak{D}\circ}, \phi\right)} \\ &\quad\times \left|\frac{\left(m_\alpha + m_{\mathrm{n}}\right) E_{\mathrm{n}} + \left(m_\alpha - m_{\mathfrak{D}}\right) E_{\mathfrak{D}\circ} + m_\alpha Q}{4\sqrt{m_{\mathfrak{D}} E_{\mathfrak{D}\circ} m_{\mathrm{n}} E_{\mathrm{n}}^3}\sin\lambda_{\mathfrak{D}\circ}\sin\phi}\right|\end{aligned} \tag{27}$$

which is the neutron energy spectrum generated by a fast deuterium cold ring and stationary tritium. The spectrum is two times the total derivative of the detected neutron rate with respect to the neutron energy E_{n}. In figure 4, we show the main terms of equation (27), where we separated the Jacobian term with the chain rule according to equation (25), for a set of different fast deuterium cold ring energies $E_{\mathfrak{D}\circ}$. For simplicity, we set the pitch angle $\lambda_{\mathfrak{D}\circ}$ and the LOS angle ϕ to $\pi/2$. We note in this case how the differential cross section and the $1/\cos\gamma_{\mathfrak{D}}$ term are skewed towards up-shifted energies. On the other hand, the Jacobian $|\mathrm{d}\sin\gamma_{\mathfrak{D}}/\mathrm{d}E_{\mathrm{n}}|$ is biased towards down-shifted neutron energies. We investigate this behaviour in section 3.3, and show the complete spectral shape in section 4.

In the following section, we interpret the information contained in equation (27) by observing how spectra are formed during neutron detection experiments and how the emission probability in the laboratory frame affects the spectral shape.

3.2. Spectra with finite resolution

Having derived the analytical formulation for the 'building block' of any neutron energy spectrum, we want to investigate how this theoretical model reflects the physics of neutron detection in a real-life experiment. In particular, we highlight that the detected spectrum will not be the exact derivative of the neutron rate—as described in section 3—since the spectral resolution of a real instrument is never infinite. The intrinsic binning of the detected energy coordinate leads to an approximation of this derivative. We can reflect this fact mathematically by expressing the resolution in terms of bin-width ΔE_{n} and considering the detected neutron rate equation (24) for a certain energy bin centred at E'_{n}, which reads

$$\begin{aligned}&\frac{\mathrm{d}n}{\mathrm{d}t}\left(E'_{\mathrm{n}} - \Delta E_{\mathrm{n}}/2 < E'_{\mathrm{n}} < E'_{\mathrm{n}} + \Delta E_{\mathrm{n}}/2\right) = \frac{\Delta\Omega_{\mathrm{lab}}}{2\pi^2} \\ &\quad\times n_{\mathfrak{D}} n_{\mathrm{T}} v_{\mathfrak{D}\circ} \int_{E'_{\mathrm{n}} - \Delta E_{\mathrm{n}}/2}^{E'_{\mathrm{n}} + \Delta E_{\mathrm{n}}/2} \frac{\mathrm{d}\sigma\left(v_{\mathfrak{D}\circ}, \lambda_{\mathfrak{D}\circ}, \gamma_{\mathfrak{D}}\left(E_{\mathrm{n}}\right), \phi\right)}{\mathrm{d}\cos\theta_{\mathrm{lab}}} \\ &\quad\times \left|\frac{\mathrm{d}\gamma_{\mathfrak{D}}}{\mathrm{d}E_{\mathrm{n}}}\right|_{v_{\mathfrak{D}\circ}, \lambda_{\mathfrak{D}\circ}, \phi} \mathrm{d}E_{\mathrm{n}}\,,\end{aligned} \tag{28}$$

or, after changing the integration variable back to $\gamma_{\mathfrak{D}}$:

$$\begin{aligned}&\frac{\mathrm{d}n}{\mathrm{d}t}\left(E'_{\mathrm{n}} - \Delta E_{\mathrm{n}}/2 < E'_{\mathrm{n}} < E'_{\mathrm{n}} + \Delta E_{\mathrm{n}}/2\right) = \frac{\Delta\Omega_{\mathrm{lab}}}{2\pi^2} \\ &\quad\times n_{\mathfrak{D}} n_{\mathrm{T}} v_{\mathfrak{D}\circ} \int_{\gamma_{\mathfrak{D}}\left(E'_{\mathrm{n}} + \Delta E_{\mathrm{n}}/2\right)}^{\gamma_{\mathfrak{D}}\left(E'_{\mathrm{n}} - \Delta E_{\mathrm{n}}/2\right)} \frac{\mathrm{d}\sigma\left(v_{\mathfrak{D}\circ}, \lambda_{\mathfrak{D}\circ}, \gamma_{\mathfrak{D}}\left(E_{\mathrm{n}}\right), \phi\right)}{\mathrm{d}\cos\theta_{\mathrm{lab}}} \\ &\quad\times \mathrm{d}\gamma_{\mathfrak{D}}\,.\end{aligned} \tag{29}$$

Equations (28) and (29) most closely resemble energy-resolved counting experiments performed with a spectrometer

with resolution ΔE_n, whenever the response function is sufficiently narrow. The response function of a spectrometer accounts for the detection physics and the corresponding broadening of the signal along E_n, i.e. the detected energy. The functional dependency can vary significantly from an instrument to another. As long as the response is Gaussian-like, and sufficiently narrow (as it can be the case for neutron diamond detectors [36] [7]), then equations (28) and (29) are a good proxy. The calculation becomes a numerical integration of the differential cross section for each energy bin of the diagnostic according to equation (29). Moreover, standard Monte Carlo simulations work similarly, where N gyro-samples are converted into N neutron energies, assigned a specific weight according to the differential reactivity $\mathrm{d}\sigma_\mathrm{lab} v_\mathrm{rel}$ and then histogrammed with a specific energy bin-width ΔE_n. The spectrum, as in the volumetric neutron rate per unit energy, is recovered by dividing the volumetric rate equation (28) by the bin-width and considering the limit of infinite resolution:

$$\begin{aligned}\lim_{\Delta E_\mathrm{n}\to 0}\frac{1}{\Delta E_\mathrm{n}}\frac{\mathrm{d}n}{\mathrm{d}t}\left(E'_\mathrm{n}-\Delta E_\mathrm{n}/2<E'_\mathrm{n}<E'_\mathrm{n}+\Delta E_\mathrm{n}/2\right)\\ =\frac{\Delta\Omega_\mathrm{lab}}{2\pi^2}n_\mathfrak{D}n_\mathrm{T}v_{\mathfrak{D}\circ}\frac{\mathrm{d}\sigma\left(v_{\mathfrak{D}\circ},\lambda_{\mathfrak{D}\circ},\gamma_\mathfrak{D}\left(E_\mathrm{n}\right),\phi\right)}{\mathrm{d}\cos\theta_\mathrm{lab}}\\ \times\left|\frac{\mathrm{d}\gamma_\mathfrak{D}}{\mathrm{d}E_\mathrm{n}}\right|_{v_{\mathfrak{D}\circ},\lambda_{\mathfrak{D}\circ},\phi}\equiv\frac{\mathrm{d}^2n}{\mathrm{d}E_\mathrm{n}\mathrm{d}t}\,.\end{aligned}\tag{30}$$

Accounting for the finite resolution of the neutron spectrometers [40] also has the advantage that the spectra do not diverge. Equation (30) diverges at the upper and lower limits of the possible neutron energies, since the probability density function of the sine function diverges. But this is of no concern, since the integrals under the curve are finite as long as the extrema are not exactly at the bin-edges $(E'_\mathrm{n}\pm\Delta E_\mathrm{n})$ in equation (29); experimentally, the number of neutrons detected by a spectrometer is finite.

3.3. The differential cross section in the centre-of-mass and laboratory frames

From equation (27), we may also note that the differential cross section for the selected reaction plays a crucial role in defining the shape of the resulting spectrum. We note that in most cases this quantity is given in terms of the cosine of the emission angle in the centre-of-mass rest frame, i.e. $\cos\theta_\mathrm{CM}$, so that tabulated data is each time transformed back into the laboratory frame—which is ultimately what one needs to compute spectra. For DD and DT reactions, the differential cross section is modelled by fitting experimental beam-target data in a reduced Legendre presentation [41, 42]

$$\begin{aligned}\frac{\mathrm{d}\sigma\left(E_\mathrm{beam},\theta_\mathrm{CM}\right)}{\mathrm{d}\cos\theta_\mathrm{CM}}=\frac{\mathrm{d}\sigma\left(E_\mathrm{beam},\cos\theta_\mathrm{CM}=1\right)}{\mathrm{d}\cos\theta_\mathrm{CM}}\\ \times\sum_l A_l P_l\left(\cos\theta_\mathrm{CM}\right)\,,\end{aligned}\tag{31}$$

where A_l is the best-fitting coefficient for the lth order Legendre polynomial P_l, while the prefactor on the right-hand side is such that $\sum_l A_l = 1$ for $\cos\theta_\mathrm{CM}=1$, and hence

$$\frac{\mathrm{d}\sigma\left(E_\mathrm{beam},\cos\theta_\mathrm{CM}=1\right)}{\mathrm{d}\cos\theta_\mathrm{CM}}=\frac{\sigma_\mathrm{tot}\left(E_\mathrm{beam}\right)}{4\pi A_0}\,.\tag{32}$$

In our case, the beam energy will be $E_\mathrm{beam}=E_\mathfrak{D}=\frac{1}{2}m_\mathfrak{D}v_\mathfrak{D}^2$ and the cosine of the emission angle needs to be transformed. The transformation from the centre-of-mass frame to the laboratory frame is given by

$$\begin{aligned}\frac{\mathrm{d}\sigma\left(v_{\mathfrak{D}\circ},\lambda_{\mathfrak{D}\circ},\gamma_\mathfrak{D}\left(E_\mathrm{n}\right),\phi\right)}{\mathrm{d}\cos\theta_\mathrm{lab}}=\frac{\mathrm{d}\sigma\left(v_{\mathfrak{D}\circ},\lambda_{\mathfrak{D}\circ},\gamma_\mathfrak{D}\left(E_\mathrm{n}\right),\phi\right)}{\mathrm{d}\cos\theta_\mathrm{CM}}\\ \times\left|\frac{\mathrm{d}\cos\theta_\mathrm{CM}}{\mathrm{d}\cos\theta_\mathrm{lab}}\right|_{v_{\mathfrak{D}\circ},\lambda_{\mathfrak{D}\circ},\gamma_\mathfrak{D}\left(E_\mathrm{n}\right),\phi}.\end{aligned}\tag{33}$$

In order to use equation (33) in the formula for the cold ring spectrum equation (27), we first need to express $\cos\theta_\mathrm{CM}$ in terms of neutron energies E_n. Additionally, we seek to evaluate the derivative with respect to $\cos\theta_\mathrm{lab}$, which is needed to express the Jacobian that governs the transformation of the solid angle (equation (9)) through the change of rest frame. We start by the definition of the cosine, namely

$$\cos\theta_\mathrm{CM}=\frac{\boldsymbol{w}_\mathrm{n}\cdot\boldsymbol{v}_\mathrm{rel}}{w_\mathrm{n}v_\mathrm{rel}}\,,\tag{34}$$

where $\boldsymbol{w}_\mathrm{n}$ is the neutron emission velocity in the centre-of-mass frame. Since $\boldsymbol{v}_\mathrm{n}=\boldsymbol{v}_\mathrm{CM}+\boldsymbol{w}_\mathrm{n}$ [21, 43], we write $\cos\theta_\mathrm{CM}$ in terms of laboratory frame velocities

$$\cos\theta_\mathrm{CM}=\frac{\left(\boldsymbol{v}_\mathrm{n}-\boldsymbol{v}_\mathrm{CM}\right)\cdot\boldsymbol{v}_\mathrm{rel}}{|\boldsymbol{v}_\mathrm{n}-\boldsymbol{v}_\mathrm{CM}|v_\mathrm{rel}}\,,\tag{35}$$

where $\boldsymbol{v}_\mathrm{CM}$ is the velocity of the centre-of-mass, assumed here as conserved throughout the reaction $\boldsymbol{v}_\mathrm{CM}\approx\boldsymbol{v}'_\mathrm{CM}$ [44]. Before making use of the beam-target approximation, we derive a general solution for equation (35) which is valid for non-stationary tritium, too. If we define χ_lab as the angle between the laboratory frame neutron velocity $\boldsymbol{v}_\mathrm{n}$ and the centre-of-mass velocity $\boldsymbol{v}_\mathrm{CM}$, then equation (35) reads

$$\cos\theta_\mathrm{CM}=\frac{v_\mathrm{n}v_\mathrm{rel}\cos\theta_\mathrm{lab}-v_\mathrm{CM}v_\mathrm{rel}\cos\left(\theta_\mathrm{lab}\pm\chi_\mathrm{lab}\right)}{v_\mathrm{rel}\sqrt{v_\mathrm{n}^2+v_\mathrm{CM}^2-2v_\mathrm{n}v_\mathrm{CM}\cos\chi_\mathrm{lab}}}\tag{36}$$

where we make implicit use of the azimuthal symmetry of the emitted neutron (i.e. at any viewing angle ϕ the emission is uniform when rotating around the magnetic field). We can therefore define θ_lab and χ_lab on the same plane, and hence the angle between the two vector velocities $\boldsymbol{v}_\mathrm{rel}$ and $\boldsymbol{v}_\mathrm{CM}$ is either the sum or the difference of the two angles θ_lab and χ_lab. We take the derivative with respect to the laboratory frame emission angle

$$\frac{\mathrm{d}\cos\theta_\mathrm{CM}}{\mathrm{d}\cos\theta_\mathrm{lab}}=\frac{v_\mathrm{n}v_\mathrm{rel}-v_\mathrm{CM}v_\mathrm{rel}\csc\left(\theta_\mathrm{lab}\right)\sin\left(\theta_\mathrm{lab}+\chi_\mathrm{lab}\right)}{v_\mathrm{rel}\sqrt{v_\mathrm{n}^2+v_\mathrm{CM}^2-2v_\mathrm{n}v_\mathrm{CM}\cos\chi_\mathrm{lab}}}\,,\tag{37}$$

which is a general relation valid also when the tritium is not stationary. For the case of beam-target reactions, the reactant relative velocity $\boldsymbol{v}_{\rm rel} \approx v_{\mathfrak{D}\circ}$ and the centre-of-mass velocity $\boldsymbol{v}_{\rm CM} \approx m_{\mathfrak{D}} v_{\mathfrak{D}\circ}/(m_{\mathfrak{D}} + m_{\rm T})$ are parallel to the fast deuterium velocity $\boldsymbol{v}_{\mathfrak{D}\circ}$. Therefore, their magnitudes can be easily computed and the angle in between them vanishes $(\theta_{\rm lab} \pm \chi_{\rm lab}) \approx 0$, further simplifying the equations. The cosine of the emission angle in the centre-of-mass rest frame equation (36) becomes

$$\begin{aligned}\cos\theta_{\rm CM} &\approx \frac{v_{\rm n} v_{\mathfrak{D}\circ}\cos\theta_{\rm lab} - \frac{m_{\mathfrak{D}}}{m_{\mathfrak{D}}+m_{\rm T}} v_{\mathfrak{D}\circ}^2}{v_{\mathfrak{D}\circ}\sqrt{v_{\rm n}^2 + \frac{m_{\mathfrak{D}}^2}{(m_{\mathfrak{D}}+m_{\rm T})^2} v_{\mathfrak{D}\circ}^2 - 2 v_{\rm n}\frac{m_{\mathfrak{D}}}{m_{\mathfrak{D}}+m_{\rm T}} v_{\mathfrak{D}\circ}\cos\theta_{\rm lab}}} \\ &= \frac{\frac{v_{\rm n}}{v_{\mathfrak{D}\circ}}\cos\theta_{\rm lab} - \frac{m_{\mathfrak{D}}}{m_{\mathfrak{D}}+m_{\rm T}}}{\sqrt{\left(\frac{v_{\rm n}}{v_{\mathfrak{D}\circ}}\right)^2 + \left(\frac{m_{\mathfrak{D}}}{m_{\mathfrak{D}}+m_{\rm T}}\right)^2 - 2\frac{m_{\mathfrak{D}}}{m_{\mathfrak{D}}+m_{\rm T}}\frac{v_{\rm n}}{v_{\mathfrak{D}\circ}}\cos\theta_{\rm lab}}}\,.\end{aligned} \tag{38}$$

By applying the derivative with respect to $\cos\theta_{\rm lab}$ now, whilst noticing that the denominator now depends on it because $\cos\chi_{\rm lab} = \cos(\pm\theta_{\rm lab})$, we can work out the simplified form of the Jacobian governing the change of rest frame in the case of a beam-target DT reaction, which reads

$$\frac{{\rm d}\cos\theta_{\rm CM}}{{\rm d}\cos\theta_{\rm lab}} \approx \frac{\frac{v_{\rm n}}{v_{\mathfrak{D}}} - \frac{m_{\mathfrak{D}}}{m_{\mathfrak{D}}+m_{\rm T}}\cos\theta_{\rm lab} - \frac{m_{\mathfrak{D}}}{m_{\mathfrak{D}}+m_{\rm T}}\frac{1}{v_{\rm n}}\left(1-\cos\theta_{\rm lab}^2\right)\frac{{\rm d}v_{\rm n}}{{\rm d}\cos\theta_{\rm lab}}}{\left(\frac{v_{\mathfrak{D}\circ}}{v_{\rm n}}\right)^2\left(\left(\frac{v_{\rm n}}{v_{\mathfrak{D}\circ}}\right)^2 + \left(\frac{m_{\mathfrak{D}}}{m_{\mathfrak{D}}+m_{\rm T}}\right)^2 - 2\frac{m_{\mathfrak{D}}}{m_{\mathfrak{D}}+m_{\rm T}}\frac{v_{\rm n}}{v_{\mathfrak{D}\circ}}\cos\theta_{\rm lab}\right)^{3/2}}. \tag{39}$$

Note that the cosine of the emission angle in the laboratory frame $\cos\theta_{\rm lab}$ is completely defined by the geometry of the problem by equation (18) and depends on the gyro-angle $\gamma_{\mathfrak{D}}$. From equation (19), we may also derive the boundaries in the centre-of-mass rest frame for the cosine of the emission angle. The domain of the emission angle in the centre-of-mass frame is going to change because of the Galilean transformation, and proportionally to the velocity of the fast ion energy as it undergoes the fusion reaction. Equation (38) gives

$$C_{\rm CM}^{\pm} = \frac{\frac{v_{\rm n}}{v_{\mathfrak{D}\circ}} C_{\rm lab}^{\pm} - \frac{m_{\mathfrak{D}}}{m_{\mathfrak{D}}+m_{\rm T}}}{\sqrt{\left(\frac{v_{\rm n}}{v_{\mathfrak{D}\circ}}\right)^2 + \left(\frac{m_{\mathfrak{D}}}{m_{\mathfrak{D}}+m_{\rm T}}\right)^2 - 2\frac{m_{\mathfrak{D}}}{m_{\mathfrak{D}}+m_{\rm T}}\frac{v_{\rm n}}{v_{\mathfrak{D}\circ}} C_{\rm lab}^{\pm}}}\,. \tag{40}$$

In figure 5, the cosine of emission angle in the centre-of-mass $\cos\theta_{\rm CM}$ and the frame change Jacobian $|{\rm d}\cos\theta_{\rm CM}/{\rm d}\cos\theta_{\rm lab}|$ are shown for a few values of the cold ring energy $E_{\mathfrak{D}\circ}$. For simplicity, the pitch angle $\lambda_{\mathfrak{D}\circ}$ and LOS angle ϕ are set to $\pi/2$. We can observe the approximately linear dependency of the cosine of the emission angle, which is shown by a first order Taylor-expansion of equation (38) for $\frac{v_{\mathfrak{D}}}{v_{\rm n}} \ll 1$. Additionally, the transformation of the solid angle is skewed towards up-shifted neutron energies, which means that the centre-of-mass probability

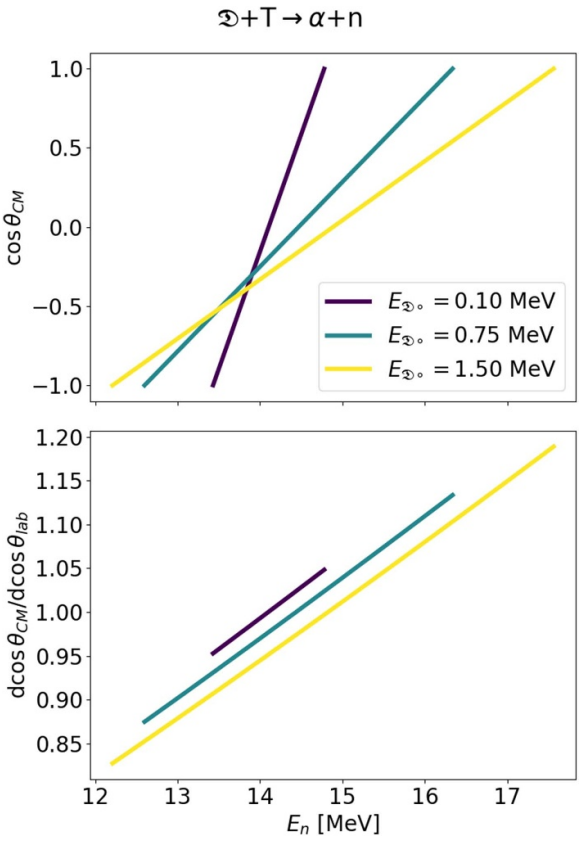

Figure 5. Cosine of emission angle in the centre-of-mass frame (top) and frame-change Jacobian (bottom) as functions of the emitted neutron energy. The calculations are shown for a set of three different deuterium cold ring energies $E_{\mathfrak{D}\circ}$. The pitch angle of the cold ring and the LOS angle are kept fixed at $\pi/2$ to avoid geometry effects.

of emission is transformed anisotropically in the laboratory frame so that forward-emission events are favoured. This effect happens independently on the actual differential cross section in the centre-of-mass and is due to the velocity of the reactant.

In figure 6, we show the differential cross section for the DT and DD reactions as functions of the cosine of the emission angle, both in the centre-of-mass frame and laboratory frame. We note how the squeezing of the solid angle between rest frames biases the probability towards forward-emission events in the laboratory frame—independently on the reaction. For completeness, we show the effect of selecting arbitrary values of cold ring pitch angle $\cos\lambda_{\mathfrak{D}}$ and viewing angle ϕ, for which the differential cross section is plotted in blue (DT) and orange (DD) circle markers: the sampled interval shrinks due to the different geometry. The circle markers are uniformly distributed in the gyro-angle coordinate $\gamma_{\mathfrak{D}}$—due to the fast deuterium gyration—but the sine function from equation (18) concentrate them at the edges of the domain.

In the next section, we proceed and perform a comparison with Monte Carlo evaluated spectra, as well as a parametric

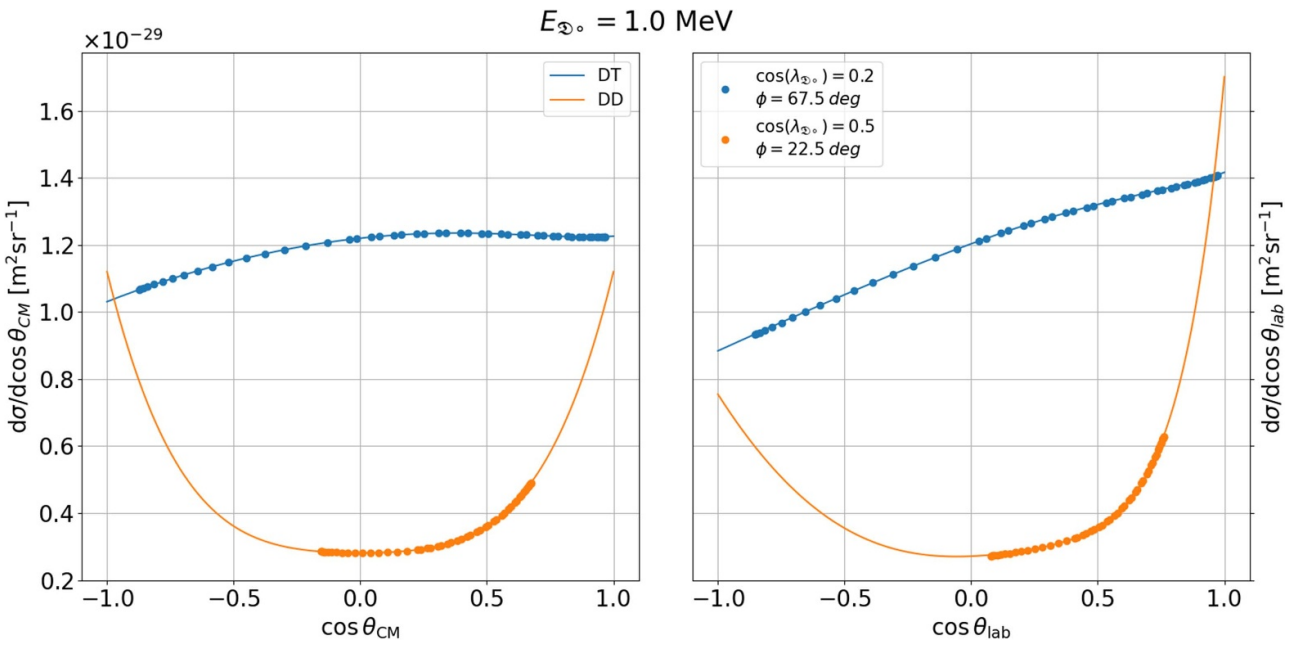

Figure 6. Differential cross section of DT (blue) and DD (orange) fusion reactions in the centre-of-mass (left panel) and laboratory (right panel) frames. The geometry is varied between the two cases to show the uneven sampling (circle markers) of the emission domain for two arbitrary geometries. The solid lines represent the complete differential cross sections in the two reference frames.

study of the spectrum with varying conditions of gyration and detection, for two selected neutronic fusion reactions.

4. Monte Carlo benchmark and parametric study

In order to validate our formula for beam-target reactions with a stationary target, a comparison with the Monte Carlo code GENESIS [21, 22] is presented. In the Monte Carlo simulation, we set the temperature of the target species to zero, and used the cold ring distribution for the beam distribution. We find a perfect match between the analytical and numerical calculations of the neutron energy spectra. We compare spectra for neutrons generated by fast deuterium reacting with stationary tritium, as well as for neutrons generated by fast deuterium reacting with stationary deuterium, as both are highly relevant processes in present and future fusion plasma experiments.

In figure 7, the fast deuterium energy is varied and the stationary target is tritium. The pitch angle $\lambda_{\mathfrak{D}\circ}$ and viewing angle ϕ are both fixed to $\pi/2$ to simplify the geometry. We observe that, as $E_{\mathfrak{D}\circ}$ increases, the range of achievable neutron energies increases—as expected; at the same time, the total cross section $\sigma_{\mathrm{lab}}^{\mathrm{tot}}$ and the relative velocity $v_{\mathrm{rel}} \approx v_{\mathfrak{D}}$ together determine the area below the spectra, which is the total neutron rate, and hence the 'height' of the spectrum. For this reaction, the negative gradient in the cross section is roughly balanced by the relative velocity contribution. The differential cross section is mostly isotropic apart from very high $E_{\mathfrak{D}\circ}$ values, at which one can see the central part of the spectrum slightly dipping downwards.

In figure 8, we investigate the DD reaction. The physics of fast ion gyration and neutron emission is the same, but the

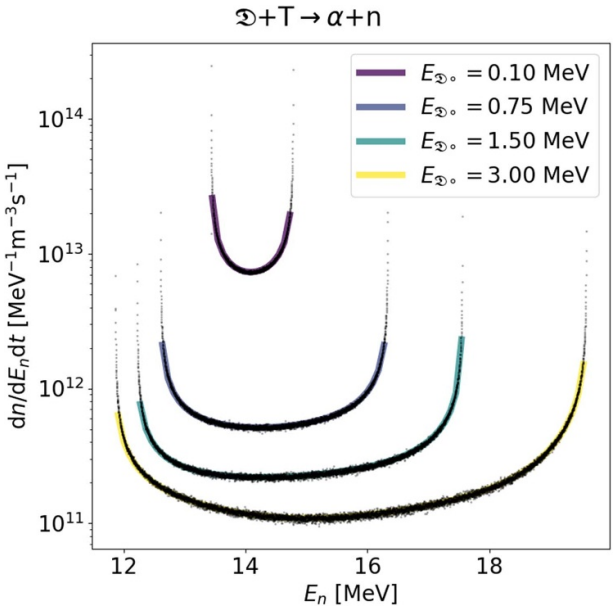

Figure 7. Neutron spectrum generated by 4 different fast deuterium cold rings reacting with stationary tritium, via $\mathfrak{D} + \mathrm{T} \rightarrow \alpha + \mathrm{n}$. Analytical calculations are compared with numerical modelling at the same conditions. The overlay between analytically calculated curves and the (black) dots obtained from the GENESIS code show extremely good agreement between the methods. $\Delta\Omega_{\mathrm{lab}} = 4\pi \times 10^{-4}$ sr; $n_{\mathfrak{D}} = 10^{18}\,\mathrm{m}^{-3}$; $n_{\mathrm{T}} = 10^{20}\,\mathrm{m}^{-3}$.

nuclear interaction between the two reactants shows a different probability distribution in the energy and in the angular coordinate. Firstly, we notice that the area under the spectrum, which is the total volumetric neutron rate, for the DD reaction varies appreciably with $E_{\mathfrak{D}\circ}$: this is due to the monotonically

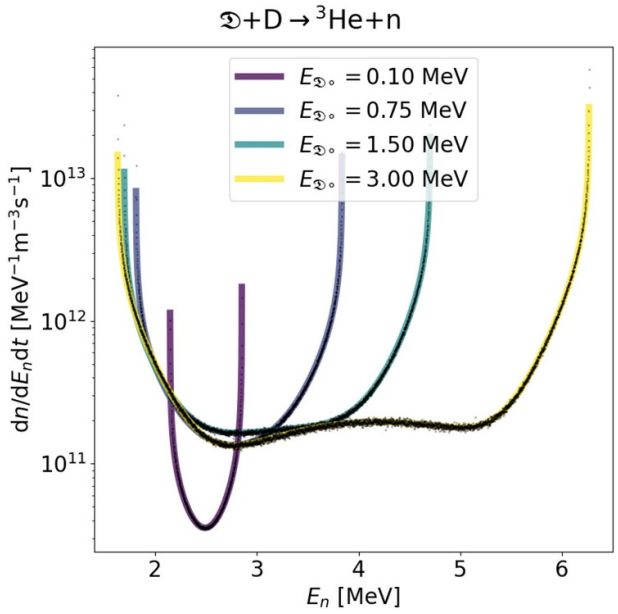

Figure 8. Neutron spectrum generated by 4 different fast deuterium cold rings reacting with stationary deuterium, via $\mathfrak{D} + \mathrm{D} \rightarrow {}^3\mathrm{He} + \mathrm{n}$. Analytical calculations are compared with numerical modelling at the same conditions. As in figure 7, the agreement with GENESIS data is very good. $\Delta\Omega_{\mathrm{lab}} = 4\pi \times 10^{-4}$ sr; $n_{\mathfrak{D}} = 10^{18}\,\mathrm{m}^{-3}$; $n_{\mathrm{D}} = 10^{20}\,\mathrm{m}^{-3}$.

strongly increasing cross section as function of the relative velocity. Secondly, we also observe the effect of an anisotropic differential cross section, which becomes more anisotropic in the angular spread as the deuterium cold ring energy increases.

In figure 9, we vary the viewing angle ϕ (top row) and the cold ring pitch angle $\lambda_{\mathfrak{D}\circ}$ (bottom row), and study the change in the spectra for the DT reaction. In this case, the fast ion energy is fixed. We first observe that the volumetric neutron rate varies because of equations (7) and (26): there is no solution in $\gamma_{\mathfrak{D}}$ for a range of emission angles $\cos\theta_{\mathrm{lab}}$, because the geometry constrains the possible values of achievable $\cos\theta_{\mathrm{lab}}$. Moreover, the model predicts identical spectra for cases *(a)* and *(b)*, which is due to an up-to-down symmetry of the system with respect to the magnetic field direction: the line-of-sight direction is specified by one angle only, namely ϕ, thanks to the azimuthal symmetry of the cross section. On the other hand, the model predicts different spectra for cases *(f)* and *(i)*, which is relevant when reconstructing fast ion distributions in velocity space. The fact that the diagnostic is sensitive to a sign-flip of the pitch value allows to distinguish co- from counter-going particles with respect to the plasma current in the case of oblique sightlines with respect to the magnetic field. This does not hold for detectors with perpendicular lines-of-sight ($\phi = \pi/2$), which are often installed or planned to be installed [45].

In figure 10 we use the same formulation as for figure 9, but for DD—varying $\lambda_{\mathfrak{D}}$ and ϕ. The main difference with DT spectra, apart from the detected neutron rate (the integral under the curve), is due to the anisotropy of the differential cross sections of the DD reaction, which becomes significant at lower energies compared to the DT reaction. This reflects onto the shape of the spectra, which are more 'corrugated' than those shown in figure 9.

By means of the Monte Carlo solver, we can also investigate how the spectral shape varies as a function of the bulk temperature T_{bulk}. We assume that a Gaussian-like beam distribution of deuterium ions interacts with a D-T plasma with bulk populations thermalized to a certain temperature T_{bulk}. The beam distribution is chosen to be centred at fast deuterium energy $E_{\mathfrak{D}} = 1\,\mathrm{MeV}$, with $\sigma_{E_{\mathfrak{D}}} = 0.04\,\mathrm{MeV}$, and to be injected with a pitch value $\cos\lambda_{\mathfrak{D}} = 0.25$, with $\sigma_{\cos\lambda_{\mathfrak{D}}} = 0.075$. The resulting spectrum is the sum of the single contributions due to the cold rings $f_{\mathfrak{D}\circ}$ that represent the entire distribution $f_{\mathfrak{D}}$. In figure 11, we show the results from the beam interacting with the tritium population for a set of different bulk temperatures, and in figure 12 analogous calculations for the beam interacting with bulk deuterium. The contribution of the isotropic Maxwellian distribution that is sampled within the Monte Carlo code results in a broadening of the spectra, which is more visible in the vicinity of the red- and blue-shift peaks of the neutron spectrum. This result is similar to what is shown in [30] for similar calculations.

The broadening of the peaks can be studied by varying both the bulk temperature and the energy of the deuterium beam that is injected. In order to do this, we consider the most sensitive cases where both the beam and the target particle are moving exactly towards the diagnostic (rightmost points in the spectra in figures 11 and 12) and both the beam and the target particle are moving away from it (leftmost points in the spectra in figures 11 and 12). Hence, we consider entirely fixed three-vector velocities here. The energy of the target particle is chosen as the average kinetic energy sampled from the Maxwellian, which corresponds to $\langle E\rangle = 3T_{\mathrm{bulk}}/2$. We evaluate the discrepancy between the Monte Carlo calculations and the beam-target model by calculating the relative difference of the most red-shifted neutron energies (bottom panel of figure 13) and of the most blue-shifted neutron energies (top panel of figure 13). The percentage relative difference, for beam energies of up 2 MeV, is below four percent in the case of bulk tritium thanks to the relatively higher Q-value of the reaction. In the case of bulk deuterium, the relative discrepancy goes up to ten percent for red-shifted neutron energies (bottom panel of figure 14), but this is mainly due to the metric we chose, which diverges for neutron energies close to zero. In absolute terms, while bulk tritium with energy $\langle E_{\mathrm{T}}\rangle = 10\,\mathrm{keV}$ leads to a maximum additional shift of $\Delta E_{\mathrm{n}} \simeq 200\,\mathrm{keV}$, the same energy for bulk deuterium only shifts the spectrum by $\Delta E_{\mathrm{n}} \simeq 60\,\mathrm{keV}$; as it can be seen from figures 11 and 12 as well.

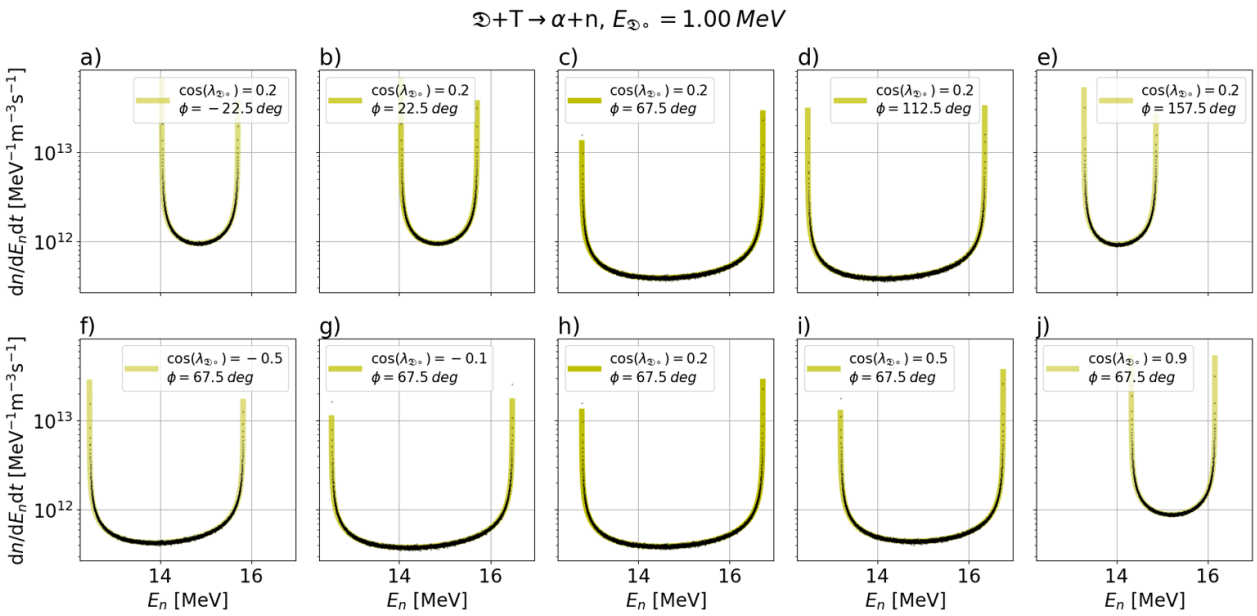

Figure 9. Parametric study of neutron spectra calculated for different values of LOS viewing angle ϕ (top row) and fast ion pitch angle $\lambda_{\mathfrak{D}\circ}$ (bottom row). Numerical modelling is also shown. The overlay between analytically calculated curves and the (black) dots obtained from the GENESIS code shows extremely good agreement between the methods. Neutrons are here produced via $\mathfrak{D} + \mathrm{T} \rightarrow \alpha + \mathrm{n}$ with fixed fast deuterium energy $E_{\mathfrak{D}\circ} = 1\,\mathrm{MeV}$. $\Delta\Omega_{\mathrm{lab}} = 4\pi \times 10^{-4}\,\mathrm{sr}$; $n_{\mathfrak{D}} = 10^{18}\,\mathrm{m}^{-3}$; $n_{\mathrm{D}} = 10^{20}\,\mathrm{m}^{-3}$.

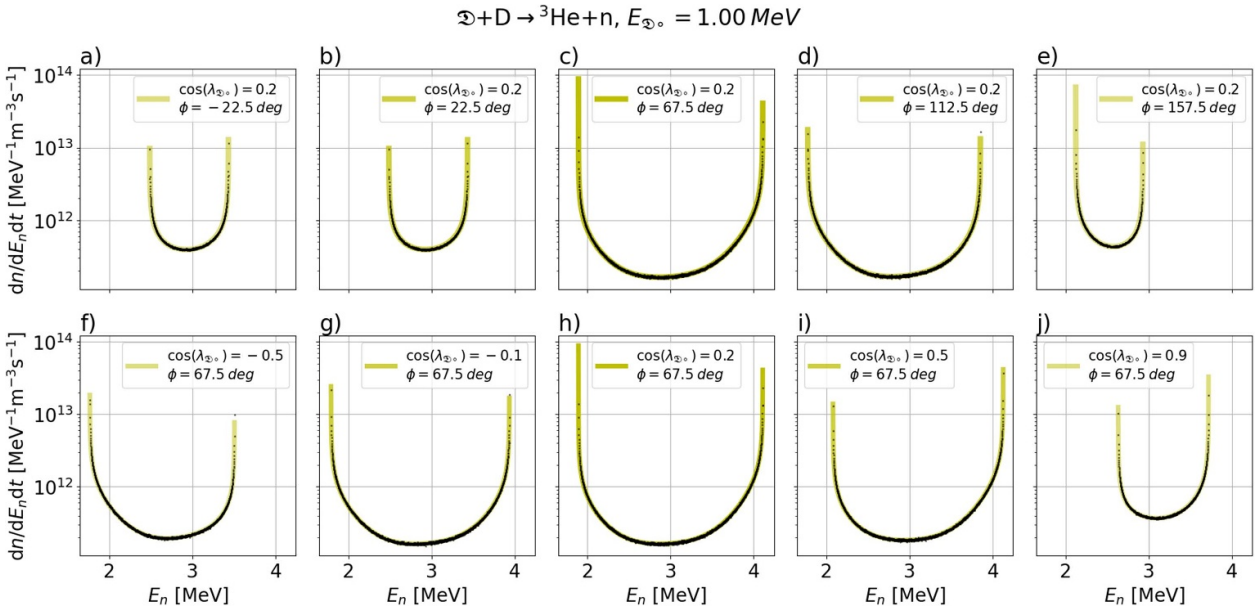

Figure 10. Parametric study of neutron spectra analytically calculated for different values of LOS viewing angle ϕ (top row) and fast ion pitch angle $\lambda_{\mathfrak{D}\circ}$ (bottom row). Numerical modelling is also shown. As in figure 9, the agreement with GENESIS data is very good. Neutrons are here produced via $\mathfrak{D} + \mathrm{D} \rightarrow {}^3\mathrm{He} + \mathrm{n}$ with fixed fast deuterium energy $E_{\mathfrak{D}\circ} = 1\,\mathrm{MeV}$. $\Delta\Omega_{\mathrm{lab}} = 4\pi \times 10^{-4}\,\mathrm{sr}$; $n_{\mathfrak{D}} = 10^{18}\,\mathrm{m}^{-3}$; $n_{\mathrm{D}} = 10^{20}\,\mathrm{m}^{-3}$.

5. Probabilistic interpretation of neutron energy spectrum formation

We may also understand the formation of neutron spectra in terms of probability density functions. In the case of bijective mapping between two variables X and Y, their probability density functions are related by [46]

$$\mathrm{pdf}_X(Y) = \mathrm{pdf}(X)\left|\frac{\mathrm{d}X}{\mathrm{d}Y}\right|, \tag{41}$$

where the subscript on the left-hand side reflects that we are given the probability distribution function of X. The neutron energy spectrum formation is determined by two probabilistic effects: the probability density of the gyro-angle $\gamma_{\mathfrak{D}}$ and

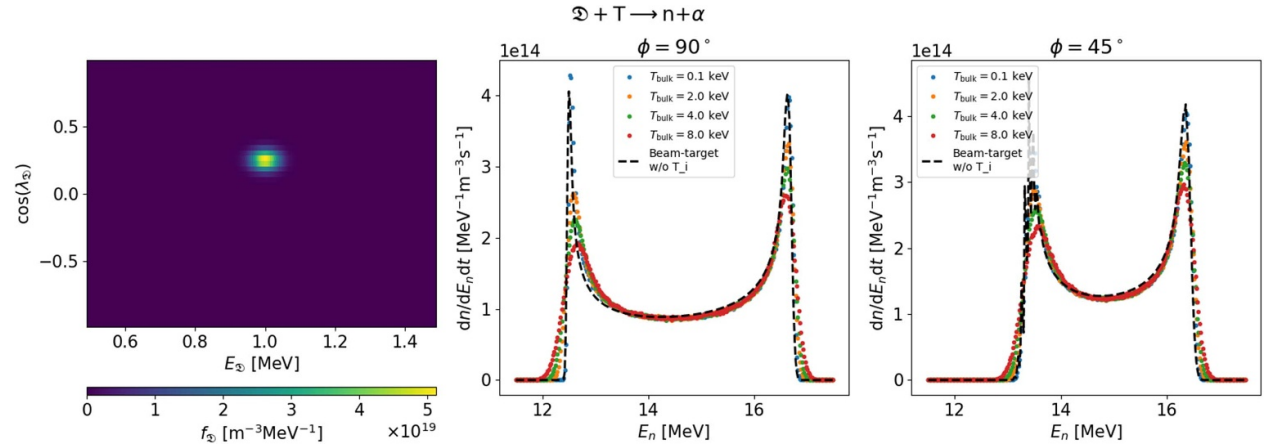

Figure 11. Neutron energy spectra generated by a beam distribution (left panel) and observed from two different viewing angle (centre and right panels). The beam-target model is compared with Monte Carlo calculations at different values of the bulk temperature T_{bulk}. Neutrons are here produced via $\mathfrak{D} + \mathrm{T} \rightarrow \alpha + \mathrm{n}$ with $\Delta\Omega_{\mathrm{lab}} = 4\pi \times 10^{-4}$ sr; $n_{\mathfrak{D}} = 5 \times 10^{17}$ m^{-3}; $n_{\mathrm{T}} = 10^{19}$ m^{-3}.

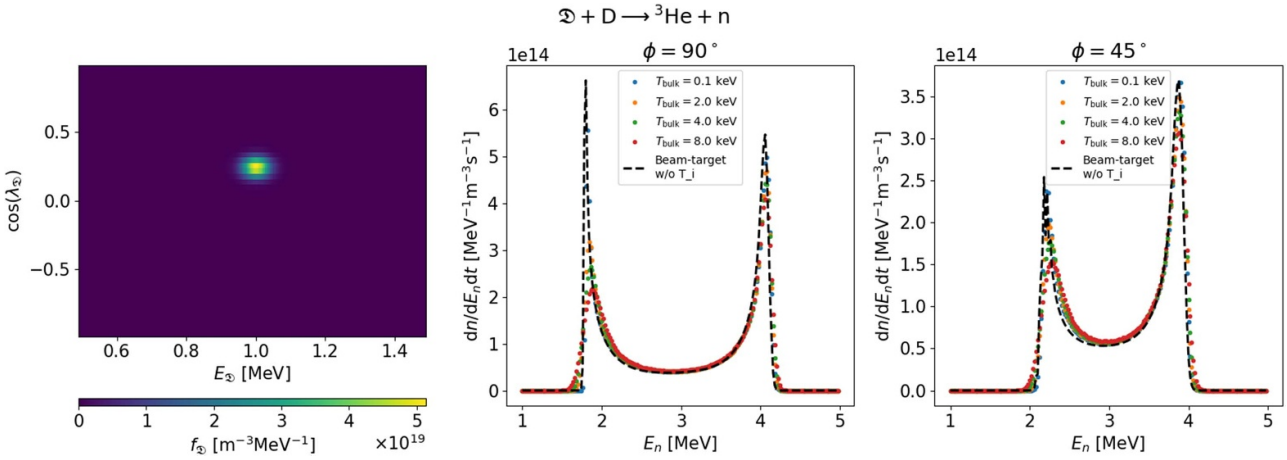

Figure 12. Neutron energy spectra generated by a beam distribution (left panel) and observed from two different viewing angle (centre and right panels). The beam-target model is compared with Monte Carlo calculations at different values of the bulk temperature T_{bulk}. Neutrons are here produced via $\mathfrak{D} + \mathrm{D} \rightarrow {}^3\mathrm{He} + \mathrm{n}$ with $\Delta\Omega_{\mathrm{lab}} = 4\pi \times 10^{-4}$ sr; $n_{\mathfrak{D}} = 5 \times 10^{17}$ m^{-3}; $n_{\mathrm{D}} = 10^{19}$ m^{-3}.

the probability density of a neutron emission along a direction with $\cos\theta_{\mathrm{lab}}$, given we have a certain gyro-angle $\gamma_{\mathfrak{D}}$. We assume probability density of the gyro-angle to be uniform. The probability of the neutron emission given a certain $\cos\theta_{\mathrm{lab}}$ and deuterium velocity $v_{\mathfrak{D}\circ}$ is quantum mechanical in nature [33, 47] and is described by the differential cross sections of the reaction.

Considering only the gyration, we can give the probability density that the fast deuterium ion has a gyro-angle $\gamma_{\mathfrak{D}}$ allowing a neutron emission with a neutron energy E_{n}

$$\begin{aligned}\mathrm{pdf}_{\gamma_{\mathfrak{D}}}(E_{\mathrm{n}}) &= \mathrm{pdf}(\gamma_{\mathfrak{D}})\left|\frac{\mathrm{d}\gamma_{\mathfrak{D}}}{\mathrm{d}E_{\mathrm{n}}}\right| \\ &= \frac{1}{\pi}\frac{1}{\cos\gamma_{\mathfrak{D}}}\left|\frac{(m_\alpha - m_{\mathrm{n}})E_{\mathrm{n}} + (m_\alpha - m_{\mathfrak{D}})\mathfrak{D}\circ + m_\alpha Q}{4\sqrt{m_{\mathfrak{D}}E_{\mathfrak{D}\circ}m_{\mathrm{n}}E_{\mathrm{n}}^3}\sin\lambda_{\mathfrak{D}\circ}\sin\phi}\right|\end{aligned} \tag{42}$$

where the gyro-angle is in the interval $\gamma_{\mathfrak{D}} \in [-\pi/2, \pi/2]$ in order to preserve bijectivity and the Jacobian is given by equation (25). This function does not account for the scattering physics of the nuclear reaction, which is reflected in the different probabilities of neutron emission for different emission angles θ_{lab}. The probability density function of a neutron emission along the line-of-sight due to a fusion reaction of a fast deuterium at gyro-angle $\gamma_{\mathfrak{D}}$ is obtained by weighting every event at $\cos\theta_{\mathrm{lab}}$ by the corresponding differential cross section value

$$\begin{aligned}\mathrm{pdf}_{\mathrm{n}\cap\gamma_{\mathfrak{D}}}(\gamma_{\mathfrak{D}}) &= \frac{1}{\mathcal{C}}\frac{\mathrm{d}\sigma(v_{\mathfrak{D}\circ}, \lambda_{\mathfrak{D}\circ}, \gamma_{\mathfrak{D}}, \phi)}{\mathrm{d}\cos\theta_{\mathrm{lab}}}\mathrm{pdf}(\gamma_{\mathfrak{D}}) \\ &= \frac{1}{\mathcal{C}}\frac{\mathrm{d}\sigma(v_{\mathfrak{D}\circ}, \lambda_{\mathfrak{D}\circ}, \gamma_{\mathfrak{D}}, \phi)}{\mathrm{d}\cos\theta_{\mathrm{lab}}}\frac{1}{\pi},\end{aligned} \tag{43}$$

where the factor $\mathcal{C}$ is needed to obey the normalization condition that the integral over the probability density function must be unity. It is obtained from the differential cross section integral over half a gyration

$$\mathcal{C} = \frac{1}{\pi}\int_{-\pi/2}^{\pi/2}\frac{\mathrm{d}\sigma(v_{\mathfrak{D}\circ}, \lambda_{\mathfrak{D}\circ}, \gamma_{\mathfrak{D}}, \phi)}{\mathrm{d}\cos\theta_{\mathrm{lab}}}\mathrm{d}\gamma_{\mathfrak{D}}\,, \tag{44}$$

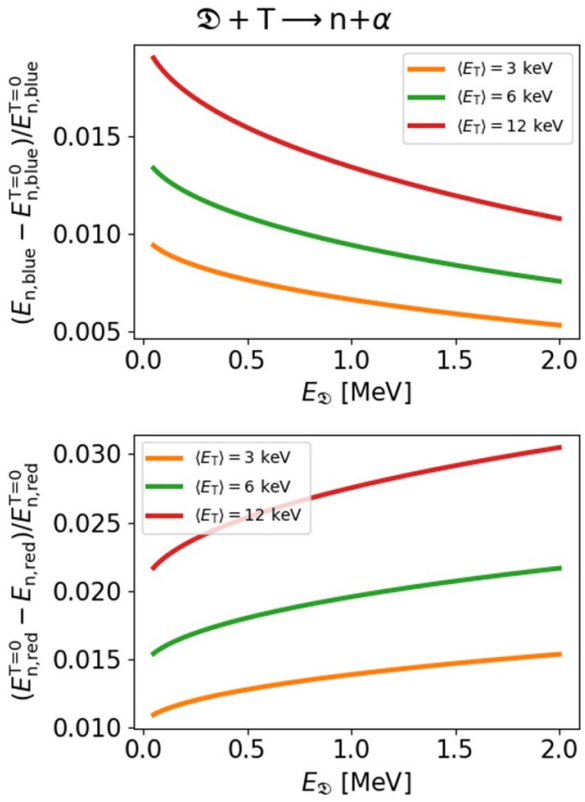

Figure 13. Relative difference between calculated blue-shifted (top panel) and red-shifted (bottom panel) neutron energies for a set of different bulk temperatures T_bulk as a function of the beam energy. Neutrons are here produced via $\mathfrak{D} + \mathrm{T} \to \alpha + \mathrm{n}$.

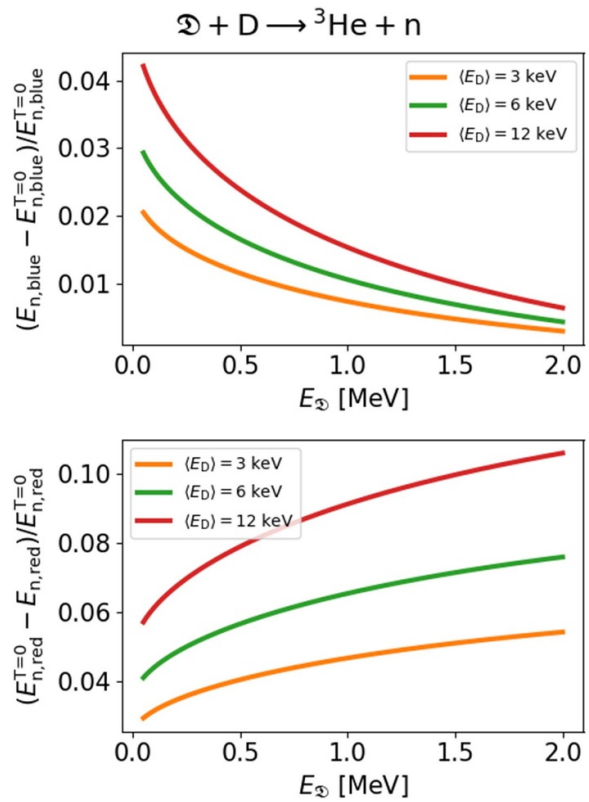

Figure 14. Relative difference between calculated blue-shifted (top panel) and red-shifted (bottom panel) neutron energies for a set of different bulk temperatures T_bulk as a function of the beam energy. Neutrons are here produced via $\mathfrak{D} + \mathrm{D} \to {}^3\mathrm{He} + \mathrm{n}$.

where the $1/\pi$ factor comes from the uniform gyration of the fast ion. We note that the integral in equation (44) does not correspond to the total cross section for any value of pitch angle $\lambda_\mathfrak{D}$ and viewing angle ϕ: all $\cos\theta_\mathrm{lab}$ value are swept if and only if both $\lambda_\mathfrak{D}$ and ϕ are equal to $\pi/2$.

We can now apply equation (41) to obtain the neutron energy probability density function for the beam-target case with a stationary target and with cold ring velocity $v_{\mathfrak{D}\circ}$, pitch angle $\lambda_{\mathfrak{D}\circ}$ and viewing angle ϕ

$$\begin{aligned}\mathrm{pdf}_{\mathrm{n}\cap\gamma_\mathfrak{D}}(E_\mathrm{n}) &= \mathrm{pdf}_{\mathrm{n}\cap\gamma_\mathfrak{D}}(\gamma_\mathfrak{D})\left|\frac{\mathrm{d}\gamma_\mathfrak{D}}{\mathrm{d}E_\mathrm{n}}\right| \\ &= \frac{1}{\mathcal{C}}\frac{\mathrm{d}\sigma(v_{\mathfrak{D}\circ},\lambda_{\mathfrak{D}\circ},\gamma_\mathfrak{D}(E_\mathrm{n}),\phi)}{\mathrm{d}\cos\theta_\mathrm{lab}}\frac{1}{\pi}\left|\frac{\mathrm{d}\gamma_\mathfrak{D}}{\mathrm{d}E_\mathrm{n}}\right|_{v_{\mathfrak{D}\circ},\lambda_{\mathfrak{D}\circ},\phi},\end{aligned} \tag{45}$$

where the gyro-angle is now a function of the neutron energy, i.e. $\gamma_\mathfrak{D} = \gamma_\mathfrak{D}(E_\mathrm{n})$.

The probability density function in equation (45) agrees with the analytical model for the neutron energy spectrum given by equation (27), recalling that the total neutron rate is given by equation (23). In fact, the normalization factor $\mathcal{C}$ is found again by integration of the differential cross section. We show this by multiplying and dividing the neutron spectrum by this factor $\mathcal{C}$ to obtain

$$\begin{aligned}\frac{\mathrm{d}^2 n}{\mathrm{d}E_\mathrm{n}\mathrm{d}t} &= \frac{\Delta\Omega_\mathrm{lab}}{2\pi^2} n_\mathfrak{D} n_\mathrm{T} v_{\mathfrak{D}\circ}\cdot\mathcal{C} \\ &\quad\times\frac{1}{\mathcal{C}}\frac{\mathrm{d}\sigma(v_{\mathfrak{D}\circ},\lambda_{\mathfrak{D}\circ},\gamma_\mathfrak{D}(E_\mathrm{n}),\phi)}{\mathrm{d}\cos\theta_\mathrm{lab}}\left|\frac{\mathrm{d}\gamma_\mathfrak{D}}{\mathrm{d}E_\mathrm{n}}\right|_{v_{\mathfrak{D}\circ},\lambda_{\mathfrak{D}\circ},\phi}.\end{aligned} \tag{46}$$

This shows that the detected neutron rate from equation (23) times the neutron energy probability density function equation (45) gives the analytic model for the energy spectrum equation (27), i.e.

$$\frac{\mathrm{d}^2 n}{\mathrm{d}E_\mathrm{n}\mathrm{d}t} = \frac{\mathrm{d}n}{\mathrm{d}t}\times\mathrm{pdf}_{\mathrm{n}\cap\gamma_\mathfrak{D}}(E_\mathrm{n}), \tag{47}$$

which completes the probabilistic interpretation of our model.

In figure 15, we compare the probability density functions of equations (42) and (45) for a set of different conditions. In the top panel, the $\mathfrak{D} + \mathrm{T} \to \alpha + \mathrm{n}$ reaction is considered, while in the bottom panel we show the same calculations for $\mathfrak{D} + \mathrm{D} \to {}^3\mathrm{He} + \mathrm{n}$.

As expected, the probability distribution for the fast ion being at a point of the gyration such that a neutron with energy E_n can be generated, i.e. the hammock-shaped functions shown in dashed lines in figure 15, is similar for the two reactions since it depends only on the particle masses but not on the nuclear reaction physics. On the other hand, the effect

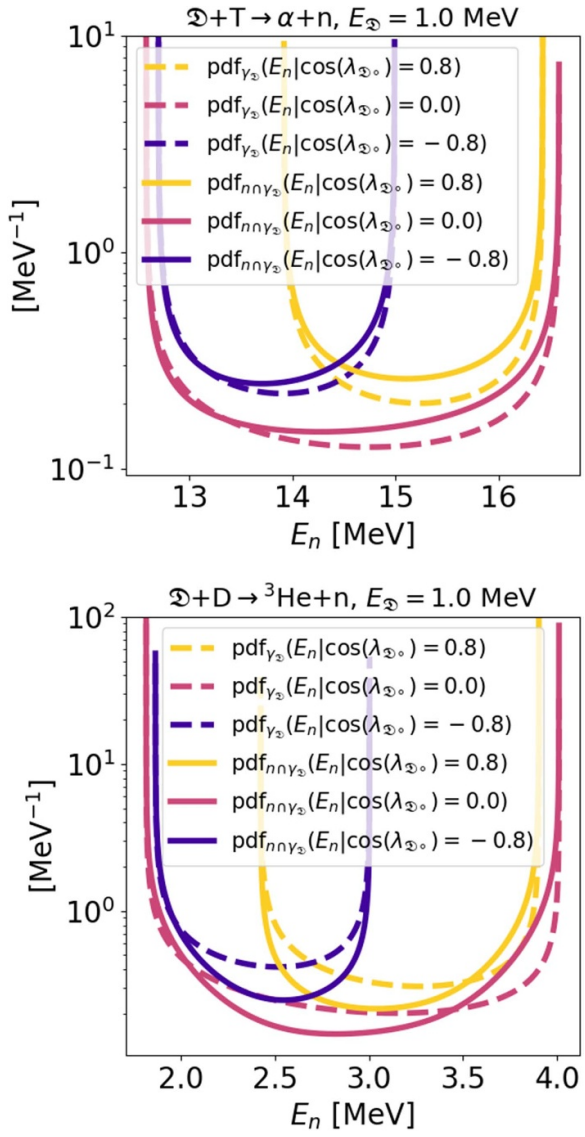

Figure 15. Probability density functions for the neutron energies E_{n} given the uniform gyration (dashed lines) and the gyration plus the reaction physics of emission (solid lines). The pitch angle $\lambda_{\mathfrak{D}}$ for the fast ion is scanned through three different values, while the viewing angle is kept at a constant value $\phi = 67.5°$. Top and bottom panel differ with the nuclear reaction which is considered: as done previously, DT (top) and DD (bottom) neutronic reactions are compared.

of the differential cross section on the probability distribution in the same energy interval is shown by the solid lines: in the case of DT neutrons, where the emission is isotropic at the energy $E_{\mathfrak{D}\circ} = 1$ MeV, one can notice how the skewing is towards up-shifted neutron energies, namely the opposite of pdf$_{\gamma_{\mathfrak{D}}}(E_{\mathrm{n}})$; this effect is mathematically reflected in the frame-change Jacobian as highlighted in section 3.3. In the case of DD neutrons, even the emission in the centre-of-mass is anisotropic and this is reflected in the shapes of the spectra (solid lines), which deviate considerably from the basic shape given by the $1/\cos\gamma_{\mathfrak{D}}$ Jacobian (figure 4) contained in the expression for this probability density function, as well as for the neutron spectra presented previously.

6. Discussion

The method presented in this work is able to rapidly compute approximate neutron energy spectra for plasmas dominated by beam-target reactions, and can be applied to study birth profiles for fusion generated populations or energy-resolved neutron fluxes impacting on wall components in fusion devices. This can be paired to existing routines for calculating analytical fast ion distributions [48] to achieve real-time predictions to be used in the control room of fusion devices. These applications will be explored in future works. In the case of fast ion diagnosis, the possibility of swiftly computing weight functions in a given magnetic equilibrium is, thanks to this new method, now within reach; for both 2D and 3D-4D applications to velocity- and position-space tomography. In the case of birth profile calculations, this can be of importance for extending the formalism to so-called two-step reactions, which in turn are especially relevant for α particle physics [45]. Finally, in the case of neutron fluxes, computational efficiency is of the utmost importance when dealing with 4D to 5D phase-spaces, as that is the case for non-axisymmetric machines such as stellarators [49].

Additionally, we remark that similar efforts have been made in the past—in the field of inertial fusion [50, 51]—to analytically or semi-analytically calculate the neutron spectra in the case of beam-target and beam-bulk reactions. Analogous work in the field of magnetic confinement [44, 52] and magneto-inertial [15] fusion has been made, which was referenced to in the course of the manuscript. Our method is tailored for fast ions gyrating around magnetic field lines, but further effort may be put here as well in including finite-temperature effects for the second reactant (which is assumed at rest) without loss of computational efficiency; except for a numerical integration of the angular cross section whenever it is not fully isotropic [51]. This would lead to a broadening and blurring of the hammock-shapes seen in this and in previous works [53].

7. Conclusions

This work presents a computationally efficient analytical formalism to compute neutron emission energy spectra from fusion reactions in plasmas dominated by beam-target reactions. Our model agrees with standard Monte Carlo simulations widely used for neutron energy spectrum calculations. For beam-target reactions with the second reactant at rest, our model is more accurate and several orders of magnitude faster than Monte Carlo simulations. Monte Carlo simulations remain necessary if the temperature of the second reactant is significant compared with the fast-ion energy. For beam-target dominated reactions with MeV-range ions, our assumptions are well fulfilled. A second advantage of our model is that it is analytically tractable and hence gives much more insight into the formation of spectra. We derived and pinpointed the appearance of bias towards neutron energies larger than the rest-frame energy. We further gave an alternative probabilistic interpretation of the spectrum formation.

This theoretical work aims both at a better understanding of the physics of spectra formation and at a potential application to experimental problems in need of faster and more efficient computations of energy-resolved nuclear products; for example in view of real-time computation of fusion product spectra.

Acknowledgment

This work has been carried out within the framework of the EUROfusion Consortium, funded by the European Union via the Euratom Research and Training Programme (Grant Agreement No 101052200—EUROfusion). Views and opinions expressed are however those of the author(s) only and do not necessarily reflect those of the European Union or the European Commission. Neither the European Union nor the European Commission can be held responsible for them. A.V. is also supported by the 'Grants in Aid of Research' initiative from Sigma Xi, to which we are grateful for the financial support via Grant No. G20240315-8377.

Appendix.

We show here an alternative derivation of the neutron energy spectrum, starting from a general approach also valid when the second reactant is not stationary. Generally, the neutron energy $E_{\rm n}'(\boldsymbol{v}_{\mathfrak{D}},\boldsymbol{v}_{\rm T})$ at which we evaluate the rate depends on the reactant velocities and is selected by a Dirac delta function. Equation (11) becomes

$$\frac{{\rm d}n}{{\rm d}t}\left(E_{\rm n}'\right)=\frac{1}{2\pi}\int\frac{{\rm d}\sigma\left(\boldsymbol{v}_{\rm rel}\right)}{{\rm d}\cos\theta_{\rm lab}}{\rm d}\Omega_{\rm lab}v_{\rm rel}f_{\mathfrak{D}}\left(\boldsymbol{v}_{\mathfrak{D}},\boldsymbol{r}\right)\times f_{\rm T}\left(\boldsymbol{v}_{\rm T},\boldsymbol{r}\right)\delta\left(E_{\rm n}-E_{\rm n}'\left(\boldsymbol{v}_{\mathfrak{D}},\boldsymbol{v}_{\rm T}\right)\right){\rm d}\boldsymbol{v}_{\mathfrak{D}}{\rm d}\boldsymbol{v}_{\rm T}{\rm d}E_{\rm n}\,. \tag{A.1}$$

This formulation reflects the way Monte Carlo simulations evaluate neutron energy spectra, which are in general not solvable analytically. The integration over the delta function selects the combinations of $\boldsymbol{v}_{\mathfrak{D}}$ and $\boldsymbol{v}_{\rm T}$ corresponding to a specific neutron energy $E_{\rm n}'$. The neutron energy spectrum [31] is obtained by taking the derivative with respect to the neutron energy $E_{\rm n}$ on both sides:

$$\frac{{\rm d}^2n}{{\rm d}E_{\rm n}{\rm d}t}\left(E_{\rm n}'\right)=\frac{1}{2\pi}\int\frac{{\rm d}\sigma\left(\boldsymbol{v}_{\rm rel}\right)}{{\rm d}\cos\theta_{\rm lab}}{\rm d}\Omega_{\rm lab}v_{\rm rel}f_{\mathfrak{D}}\left(\boldsymbol{v}_{\mathfrak{D}},\boldsymbol{r}\right)\times f_{\rm T}\left(\boldsymbol{v}_{\rm T},\boldsymbol{r}\right)\delta\left(E_{\rm n}-E_{\rm n}'\left(\boldsymbol{v}_{\mathfrak{D}},\boldsymbol{v}_{\rm T}\right)\right){\rm d}\boldsymbol{v}_{\mathfrak{D}}{\rm d}\boldsymbol{v}_{\rm T}\,. \tag{A.2}$$

If we plug in the fast ion cold ring distribution (equation (12)) and the stationary ion point distribution (equation (13)), and integrate over $v_{\mathfrak{D}}$, $\boldsymbol{v}_{\rm T}$ and $\cos\lambda_{\mathfrak{D}}$, we obtain, similarly to equation (22)

$$\frac{{\rm d}^2n}{{\rm d}E_{\rm n}{\rm d}t}\left(E_{\rm n}'\right)=\frac{\Delta\Omega_{\rm lab}}{4\pi^2}n_{\mathfrak{D}}n_{\rm T}v_{\mathfrak{D}\circ}\times\int_{-\pi}^{\pi}\frac{{\rm d}\sigma\left(v_{\mathfrak{D}\circ},\lambda_{\mathfrak{D}\circ},\gamma_{\mathfrak{D}},\phi\right)}{{\rm d}\cos\theta_{\rm lab}}\times\delta\left(E_{\rm n}-E_{\rm n}'\left(v_{\mathfrak{D}\circ},\lambda_{\mathfrak{D}\circ},\gamma_{\mathfrak{D}},\phi\right)\right){\rm d}\gamma_{\mathfrak{D}} \tag{A.3}$$

where we have already taken the approximately constant fraction of solid angle $\Delta\Omega_{\rm lab}$ seen by the detector out of the integral. We note that, for beam-target reactions with stationary target, we can transform the argument of the Dirac delta function from neutron energies $E_{\rm n}$ to fast deuterium gyro-angles $\gamma_{\mathfrak{D}}$ and obtain

$$\frac{{\rm d}^2n}{{\rm d}E_{\rm n}{\rm d}t}\left(E_{\rm n}'\right)=\frac{\Delta\Omega_{\rm lab}}{4\pi^2}n_{\mathfrak{D}}n_{\rm T}v_{\mathfrak{D}\circ}\times\int_{-\pi}^{\pi}\frac{{\rm d}\sigma\left(v_{\mathfrak{D}\circ},\lambda_{\mathfrak{D}\circ},\gamma_{\mathfrak{D}},\phi\right)}{{\rm d}\cos\theta_{\rm lab}}\delta\left(\gamma_{\mathfrak{D}}-\gamma_{\mathfrak{D}}'\right)\times\left|\frac{{\rm d}\gamma_{\mathfrak{D}}}{{\rm d}E_{\rm n}}\right|_{v_{\mathfrak{D}\circ},\lambda_{\mathfrak{D}\circ},\phi}{\rm d}\gamma_{\mathfrak{D}}\,. \tag{A.4}$$

In equation (A.4), we note that, similarly to equations (22) and (23), the same neutron energy $E_{\rm n}'$ is picked out twice; in this case, this effect is given by the Dirac delta transformation, which sums over all the roots of $\left(\gamma_{\mathfrak{D}}-\gamma_{\mathfrak{D}i}'\right)$

$$\delta\left(E_{\rm n}-E_{\rm n}'\right)=\sum_{i=0}\frac{\delta\left(\gamma_{\mathfrak{D}}-\gamma_{\mathfrak{D}i}'\right)}{\left|\frac{{\rm d}E_{\rm n}}{{\rm d}\gamma_{\mathfrak{D}}}\left(\gamma_{\mathfrak{D}i}'\right)\right|}\,, \tag{A.5}$$

where $\gamma_{\mathfrak{D}i}'$ are the roots of $\left(E_{\rm n}-E_{\rm n}'\right)=f(\gamma_{\mathfrak{D}})=0$. Since there are two roots, then a factor of 2 will appear as soon as we take the integral in $\gamma_{\mathfrak{D}}$:

$$\frac{{\rm d}^2n}{{\rm d}E_{\rm n}{\rm d}t}\left(E_{\rm n}'\right)=\frac{\Delta\Omega_{\rm lab}}{2\pi^2}n_{\mathfrak{D}}n_{\rm T}v_{\mathfrak{D}\circ}\times\frac{{\rm d}\sigma\left(v_{\mathfrak{D}\circ},\lambda_{\mathfrak{D}\circ},\gamma_{\mathfrak{D}}\left(E_{\rm n}'\right),\phi\right)}{{\rm d}\cos\theta_{\rm lab}}\left|\frac{{\rm d}\gamma_{\mathfrak{D}}}{{\rm d}E_{\rm n}}\right|_{v_{\mathfrak{D}\circ},\lambda_{\mathfrak{D}\circ},\phi}\,. \tag{A.6}$$

The neutron energy spectrum in equation (A.6) is identical with our equation (27), which concludes our alternative derivation.

ORCID iDs

A. Valentini https://orcid.org/0009-0003-5394-4267
B.C.G. Reman https://orcid.org/0000-0003-3507-9444
M. Nocente https://orcid.org/0000-0003-0170-5275
J. Eriksson https://orcid.org/0000-0002-0892-3358
H. Järleblad https://orcid.org/0000-0003-1126-686X
M. Rud https://orcid.org/0000-0003-2482-4461
B.S. Schmidt https://orcid.org/0000-0001-5302-9489
M. Salewski https://orcid.org/0000-0002-3699-679X

References

[1] Gaffey J.D.J. 1976 *J. Plasma Phys.* **16** 149–69
[2] Cordey J.G. and Core W.G.F. 1974 *Phys. Fluids* **17** 1626–30
[3] Fitzgerald M. *et al* (JET Contributors) 2023 *Nucl. Fusion* **63** 112006
[4] Heidbrink W.W. 2008 *Phys. Plasmas* **15** 055501
[5] Salewski M. 2019 Fast-ion diagnostic in fusion plasmas by velocity-space tomography *Technical Thesis* Technical University of Denmark
[6] Moseev D., Salewski M., Garcia-Muñoz M., Geiger B. and Nocente M. 2018 *Rev. Mod. Plasma Phys.* **2** 7
[7] Nocente M. *et al* (JET Contributors) 2022 *Rev. Sci. Instrum.* **93** 093520
[8] Salewski M. *et al* (the ASDEX Upgrade Team) 2014 *Nucl. Fusion* **54** 023005
[9] Salewski M. *et al* (the ASDEX Upgrade Team) 2016 *Nucl. Fusion* **56** 106024
[10] Salewski M. *et al* (JET Contributors) 2017 *Nucl. Fusion* **57** 056001
[11] Stagner L., Heidbrink W.W., Salewski M., Jacobsen A.S. and Geiger B. (DIII-D Team and ASDEX Upgrade Team) 2022 *Nucl. Fusion* **62** 026033
[12] Eriksson J. *et al* 2019 *Plasma Phys. Control. Fusion* **61** 014027
[13] Rigamonti D. *et al* (JET Contributors) 2024 *Nucl. Fusion* **64** 016016
[14] Eriksson J., Conroy S., Andersson Sundén E. and Hellesen C. 2016 *Comput. Phys. Commun.* **199** 40–46
[15] Knapp P.F., Sinars D.B. and Hahn K.D. 2013 *Phys. Plasmas* **20** 062701
[16] Jacobsen A.S., Binda F., Cazzaniga C., Eriksson J., Hjalmarsson A., Nocente M., Salewski M. and Tardini G. 2017 *Rev. Sci. Instrum.* **88** 073506
[17] Nocente M., Källne J., Salewski M., Tardocchi M. and Gorini G. 2015 *Nucl. Fusion* **55** 123009
[18] Heidbrink W.W., Garcia A., Boeglin W. and Salewski M. 2021 *Plasma Phys. Control. Fusion* **63** 055008
[19] Salewski M. *et al* 2015 *Nucl. Fusion* **55** 093029
[20] Moseev D. and Salewski M. 2019 *Phys. Plasmas* **26** 020901
[21] Nocente M. 2011 Neutron and gamma-ray emission spectroscopy as fast ion diagnostics in fusion plasmas *PhD Thesis* University of Milano Bicocca
[22] Nocente M. *et al* (JET Contributors E) 2012 *Nucl. Fusion* **52** 063009
[23] Maslov M. *et al* (JET Contributors) 2023 *Nucl. Fusion* **63** 112002
[24] Jacobsen A.S., Salewski M., Eriksson J., Ericsson G., Korsholm S.B., Leipold F., Nielsen S.K., Rasmussen J. and Stejner M. (EFDA JET Contributors) 2015 *Nucl. Fusion* **55** 053013
[25] Valentini A., Reman B.C.G., Nocente M., Eriksson J., Järleblad H., Moseev D., Rud M., Snicker A. and Salewski M. 2024 *Rev. Sci. Instrum.* **95** 083551
[26] Appelbe B. and Chittenden J. 2014 *High Energy Density Phys.* **11** 30–35
[27] Munro D.H. 2016 *Nucl. Fusion* **56** 036001
[28] Ballabio L., Källne J. and Gorini G. 1998 *Nucl. Fusion* **38** 1723–35
[29] Salewski M. *et al* 2011 *Nucl. Fusion* **51** 083014
[30] Hellesen C. (EFDA JET Contributors) 2013 *Nucl. Fusion* **53** 113009
[31] Eriksson J. 2010 Calculations of neutron energy spectra from fast ion reactions in tokamak fusion plasmas *Master's Thesis* Uppsala Univesitet
[32] Jackson J.D. 1999 *Classical Electrodynamics* 3rd edn (Wiley)
[33] Goldhaber M. and Fowler R.H. 1934 *Proc. Camb. Phil. Soc.* **30** 561
[34] Järleblad H., Stagner L., Salewski M., Eriksson J., Benjamin S., Madsen B., Nocente M., Rasmussen J. and Schmidt B.S. 2021 *Rev. Sci. Instrum.* **92** 043526
[35] Järleblad H., Stagner L., Salewski M., Eriksson J., Nocente M., Rasmussen J., Stancar Z., Kazakov Y.O. and Simmendefeldt B (JET Contributors) 2022 *Nucl. Fusion* **62** 112005
[36] Rud M. *et al* 2024 *Nucl. Fusion* **64** 036007
[37] Bosch H.S. and Hale G.M. 1992 *Nucl. Fusion* **32** 611–31
[38] Gamow G. 1928 *Z. Phys.* **51** 204–12
[39] Järleblad H., Stagner L., Salewski M., Eriksson J., Nocente M., Schmidt B.S. and Rud Larsen M. 2024 *Comput. Phys. Commun.* **294** 108930
[40] Nocente M. *et al* 2017 *Nucl. Fusion* **57** 076016
[41] Liskien H. and Paulsen A. 1973 *Nucl. Data Tables* **11** 569
[42] Drosg M. 2015 Evaluation of the absolute angle-dependent differential neutron production cross sections by the reactions 3H(p,n)3He, 1H(t,n)3He, 2H(d,n)3He, 3H(d,n)4He, and 2H(t,n)4He and of the cross sections of their time-reversed counterparts up to 30 MeV and beyond *Technical Report* IAEA Nuclear Data section
[43] Landau L.D., Lifshitz E.M. and Donnelly R.J. 1972 *Am. J. Phys.* **40** 1050–1
[44] Brysk H. 1973 *Plasma Phys.* **15** 611–7
[45] Salewski M. *et al* 2018 *Nucl. Fusion* **58** 096019
[46] Grimmett G. and Stirzaker D. 2001 *Probability and Random Processes* (Oxford University Press)
[47] Baylor L. *et al* 2023 *Nucl. Fusion* **63** 076009
[48] Weiland M., Bilato R., Dux R., Geiger B., Lebschy A., Felici F., Fischer R., Rittich D. and van Zeeland M. (the ASDEX Upgrade Team and the Eurofusion MST1 Team) 2018 *Nucl. Fusion* **58** 082032
[49] Schmidt B.S. *et al* (W7-X Team) 2023 *Nucl. Fusion* **63** 076016
[50] Appelbe B. and Chittenden J. 2011 *Plasma Phys. Control. Fusion* **53** 045002
[51] Appelbe B. and Chittenden J. 2012 *Phys. Plasmas* **19** 073115
[52] Bernstein M.J. and Comisar G.G. 1972 *Phys. Fluids* **15** 700–7
[53] Salewski M. *et al* 2016 *Nucl. Fusion* **56** 046009